lubricants

MDPI

Article

Machinability Assessment of Forged, SLM and Heat-Treated Inconel 718 Under Dry and MQL Conditions Using Machine Learning Models

Fulya Cemaloğlu [1,2], Barış Özlü [3], Halil Demir [4] and Fuat Kara [5,*]

[1] Manufacturing Engineering, Institute of Graduate Education, Karabük University, Karabük 78050, Turkey; fulya.cirakoglu@erzincan.edu.tr
[2] Department of Machinery and Metal Technologies, Vocational High School, Erzincan Binali Yıldırım University, Erzincan 24002, Turkey
[3] Department of Machine and Metal Technology, Technical Sciences Vocational School, Aksaray University, Aksaray 68100, Turkey; barisozlu@aksaray.edu.tr
[4] Department of Mechanical Engineering, Faculty of Engineering and Natural Sciences, Karabük University, Karabük 78050, Turkey; hdemir@karabuk.edu.tr
[5] Department of Mechanical Engineering, Engineering Faculty, Düzce University, Düzce 81620, Turkey
* Correspondence: fuatkara@duzce.edu.tr

Abstract

In this study, the milling performance of Inconel 718 alloys produced by forging (WP1), Inconel 718 produced by Selective Laser Melting (SLM) (WP2), and Inconel 718 (WP3) subjected to heat treatment after SLM, under different cooling/lubrication conditions, was evaluated using experimental and artificial intelligence-based approaches. Microstructural analysis showed a homogeneous fine-grained structure in WP1, while WP2 exhibited dendritic features and porosity. Heat treatment improved the microstructural homogeneity of WP3. The hardness values of WP1, WP2, and WP3 were 457 Hv, 303.33 Hv, and 391 Hv, respectively. Milling experiments yielded cutting forces of 336.5–1185.9 N, surface roughness values of 0.22–1.39 µm, and cutting temperatures of 168–658 °C. Compared with dry machining, MQL reduced average cutting force and cutting temperature by 15.5% and 18.65%, respectively, while improving tool wear and surface integrity. Machine learning models including LR, DTR, SVR, and GPR were developed to predict machining responses. GPR provided the highest prediction accuracy, achieving 98.72% for cutting force and 98.99% for cutting temperature. The results demonstrate that manufacturing route and cooling strategy significantly affect the machinability of Inconel 718 and that machine learning techniques can effectively support machining process optimization.

Keywords: Inconel 718 Selective Laser Melting; microstructure and mechanical properties; cutting force; surface roughness; tool wear; machine learning

Check for updates

Received: 20 May 2026
Revised: 27 June 2026
Accepted: 29 June 2026
Published: 1 July 2026

Copyright: © 2026 by the authors. Licensee MDPI, Basel, Switzerland. This article is an open access article distributed under the terms and conditions of the Creative Commons Attribution (CC BY) license.

1. Introduction

Additive Manufacturing (AM) enables the fabrication of complex geometries and internal structures that are difficult or impossible to produce using conventional manufacturing methods while providing significant design flexibility [1,2]. Additive manufacturing is known to have excellent potential for reducing both the production time and cost of a product. Various processes can be chosen within this technology, and the fundamental factor distinguishing these processes is how the material is built in layers [3]. Metal-based additive manufacturing is an advanced manufacturing method in which three-dimensional

(3D) objects are produced by melting metallic material, in the form of wire or powder, in layers using an energy source [4]. Selective Laser Melting (SLM) is one of the most frequently preferred techniques in the production of metallic materials. In this production process, metal powders are generally used as raw materials, and these powders are melted using a focused laser source. The molten material subsequently solidifies to form the final component [5]. Inconel 718 is a nickel-based superalloy widely used in aerospace, energy, and nuclear applications because of its excellent mechanical strength, corrosion resistance, and high-temperature performance. The Inconel 718 superalloy, containing a Ni-Cr-Fe austenite (γ) matrix, stands out with its high strength, high temperature resistance, and high corrosion resistance. Despite these advantages, Inconel 718 is considered a difficult-to-machine material. It hardens easily during processing and maintains its structural strength at very high temperatures. Furthermore, the abrasive carbides it contains increase the wear rate of cutting tools, and due to its low thermal conductivity, it causes sudden temperature changes at the tool–chip interface, thus shortening tool life. Additive manufacturing, particularly the SLM process, provides an alternative route for producing complex Inconel 718 components [6–9].

Heat treatments applied to Inconel 718 alloy produced by SLM significantly transform the material's microstructure, depending on the processing conditions. Heat treatment is commonly applied to homogenize the microstructure, promote the precipitation of strengthening γ' and γ'' phases, reduce brittle secondary phases, and relieve residual stresses. The dominant phases in untreated SLM-produced Inconel 718 alloy are the matrix phase and brittle Laves phases. When only double aging is applied, although the reinforcing phases increase, the Laves phase remains largely unchanged in the structure. However, when high-temperature solution treatment followed by aging is applied, the brittle Laves phase disappears, and the amount of γ' (Ni3(Ti, Al)) and γ'' (Ni3Nb) phases, which provide strength to the material, increases much more significantly. The substructures and stress concentrations created in the material by the SLM production method are successfully reduced through heat treatments [8,10].

Machine learning techniques have recently been employed to predict machining responses and optimize process parameters. Methods such as Linear Regression (LR), Support Vector Regression (SVR), Artificial Neural Networks (ANNs), and Adaptive Neuro-Fuzzy Inference Systems (ANFISs) have demonstrated promising performance in modeling complex relationships between machining inputs and outputs. In addition, statistical approaches such as the Taguchi method remain widely used for process optimization [11–14]. In addition to data-driven machine learning approaches, physics- and mechanics-based machining models remain fundamental tools for predicting machining responses and understanding the underlying cutting mechanisms. Mechanistic models establish analytical relationships between cutting parameters, tool geometry, and material behavior, thereby providing physically interpretable predictions of machining forces and process dynamics. Recent studies have demonstrated that these theoretical approaches can effectively complement machine learning techniques by improving the physical understanding and reliability of machining process prediction [15].

Studies comparing the machinability performance of Inconel 718 alloy produced by additive manufacturing methods after heat treatment with that of Inconel 718 alloy produced by forging methods were examined in the literature. The examination revealed that studies focused on cutting tool geometry, cutting tool coating, minimum lubricant amount, different cooling/lubrication techniques, and vibration. The current studies focus on the effects of machining parameters on mechanical (cutting forces, surface roughness values) and thermal (cutting temperature, tool wear amount) outputs, and on the optimization of these processes [16–18]. Natarajan et al. found that the best performance in machining Inconel

718 was obtained with SLM (HIP+AHT) specimens, while carbides with a size of 5–30 µm in specimens produced by conventional methods accelerated wear and increased the cutting force by 20% [18]. Schulze et al. showed that in milling SLM Inconel 718 alloy, negative rake angle (−12°) cutting tools and large helix angles accelerate tool wear by causing build-up chip formation (BUE), while the lowest wear was obtained with cutting tools having a 9° clearance angle. Furthermore, it was emphasized that multilayer TiAlN+TiAl coatings significantly increased tool life [19]. Bagherzadeh et al. demonstrated that the low shear angle generated during machining of Inconel 718 alloy produced by SLM results in higher cutting forces and consequently lower power consumption compared to forged parts. Furthermore, it was determined that increasing cutting speeds reduced the forces, while high feed rates and cooling conditions increased shear stress, thereby increasing cutting forces [20]. Periane et al. emphasized that in machining Inconel 718, the material's manufacturing method has a greater impact on tool life than cooling conditions. Parts produced using the SLM method have a longer tool life compared to parts produced using conventional methods (80% longer in dry cutting and 43% longer in MQL). However, machinability tests have shown that using MQL causes chip segmentation and leads to mechanical fractures, thus reducing tool life compared to dry machining [21]. Khanna et al. emphasized that the flank geometry and coating type directly affect the performance of Inconel 718 alloy produced by wire arc welded additive manufacturing (WAAM) in dry drilling operations. In the same study, it was reported that TiN-coated drill bits yielded the best results with superior surface integrity and low power consumption, while TiAlN-coated tools significantly reduced machinability performance by increasing wear and power consumption [22]. Careri et al. reported that in dry turning experiments on Inconel 718 alloy produced by Directed Energy Deposition (DED), low machining parameters (0.1 mm/tooth feed rate and 70 m/min cutting speed) provided optimum surface quality. However, increasing these values to 0.2 mm/tooth and 120 m/min, respectively, accelerated cutting tool wear in heat-treated specimens, increasing surface roughness values. In contrast, non-heat-treated DED parts exhibited acceptable surface roughness values despite these increased cutting speeds and feed rates [23]. Chen et al. observed that the high density and hardness of forged Inconel 718 alloy caused excessive cutting vibrations during machining, whereas the lower density and hardness of Inconel 718 alloy produced by Laser Additive Manufacturing (LAM) reduced vibrations by approximately 17%, regardless of the cutting tool's properties [24]. Tian et al. reported that in grinding Inconel 718 alloy produced by the SLM method, the surface quality directly varies depending on the grinding direction due to the anisotropic microstructure of the material. When the grinding process is performed in the scanning direction of the laser (X-axis), a smoother and more stable surface is obtained compared to the build direction (Z-axis) because the abrasives cross fewer layer boundaries, creating lower force fluctuations. In addition, it was reported that as the grinding speed increases, the average surface roughness value increases, and the difference in surface quality between these two axes also gradually increases [25]. Calleja et al. investigated the machinability of Inconel 718 alloy, produced by direct energy deposition (DED), using both turning and milling methods. The study reported that cutting forces were lower when machining nickel-based alloys produced by DED, while cutting forces were higher in heat-treated alloys [26]. Kaynak et al. investigated the effect of feed rate on surface roughness values in the turning of Inconel 718 alloy produced by the SLM method. They reported that in the turning operations, increasing feed rate, although leading to surface hardening, resulted in a reduction of over 90% in average surface roughness values [27].

Recent studies have also demonstrated the effectiveness of machine learning techniques, including Random Forest, Artificial Neural Networks, and regression-based models,

for predicting the mechanical properties and manufacturing performance of additively manufactured Inconel 718 [28–31].

Numerous studies exist in the literature evaluating the machinability performance of Inconel 718 alloy produced by different manufacturing methods. However, studies focusing on modeling and predicting input-output parameters using machine learning-based approaches in evaluating the machinability performance of Inconel 718 alloy obtained by different manufacturing methods are still limited. In particular, research that comprehensively analyzes the effects of microstructural and mechanical differences arising from manufacturing methods on machining performance using data-driven methods is insufficient in the literature.

In the studies conducted, the effects of microstructure, mechanical properties, cooling/lubrication conditions, and cutting parameters on cutting force, surface roughness, cutting temperature, and tool wear were investigated in detail during the milling of Inconel 718 specimens produced by forging and SLM methods, as well as specimens subjected to heat treatment after SLM. Furthermore, in the present study, machine learning algorithms will be trained using cutting force, surface roughness, and cutting temperature data generated during the milling of Inconel 718 specimens produced by forging and SLM methods, and specimens subjected to heat treatment after SLM. The aim of developing these predictive models is to predict the outputs of parameter combinations not included in the experimental matrix and to subject the obtained predictions to a comparative analysis by validating them with existing experimental findings. It is expected that the findings will contribute to process optimization in advanced engineering applications such as the aerospace, defense, and energy industries where Inconel 718 alloy is widely used, and will constitute an important reference for future academic studies in this field.

2. Materials and Methods

2.1. Workpiece, Machine Tool and Cutting Tool

In the milling experiments, forged Inconel 718 (WP1) and Selective Laser Melted (SLM) Inconel 718 (WP2) were used as workpiece materials. To obtain the third workpiece material (WP3), one of the SLM-produced specimens was subjected to homogenization heat treatment at 980 °C for 1.5 h, followed by air cooling. Subsequently, the specimen was aged at 800 °C for 4 h and air cooled to complete the heat-treatment process. The chemical compositions of the workpiece materials are presented in Table 1.

Table 1. Chemical compositions of the WP1 and WP2 alloys.

Workpieces	Elements											
	Ni	**Fe**	**Cr**	**Nb**	**Mo**	**Mn**	**Ti**	**Al**	**C**	**Si**	**Co**	**W**
WP1	52.98	19.62	17.55	4.840	3.140	0.046	1.030	0.550	0.087	0.076	0.076	0.000
WP2	54.40	18.45	18.14	3.770	2.830	0.039	1.240	0.430	0.284	0.199	0.136	0.084

The forged WP1 specimen was commercially supplied in dimensions of 25 mm × 25 mm × 55 mm and subsequently milled to 22 mm × 22 mm × 55 mm prior to the experiments. In contrast, WP2 and WP3 specimens were manufactured directly in dimensions of 22 mm × 22 mm × 55 mm using an Enavision 250 SLM (Ermaksan, Bursa, Turkey) machine with a laser power of 220 W, scanning speed of 800 mm/s, layer thickness of 0.03 mm, scan interval of 0.1 mm, and layer rotation angle of 67°. Milling experiments were conducted on a Johnford VMC 550 CNC (Johnford, Taichung, Taiwan) vertical machining center (7.5 kW) equipped with a Fanuc control unit. Coated carbide inserts (EDPT140408PDSRGE, KCSM40 grade) manufactured by Kennametal (Kennametal Inc., Pittsburgh, PA, USA) were used as

cutting tools. The inserts featured a 90° approach angle, a corner radius of 0.8 mm, and a PVD TiAlN/TiN coating. The inserts were mounted on a Kennametal 25A03R044B25SED14 tool holder. Detailed specifications and images of the cutting tool assembly are provided in Figure 1.

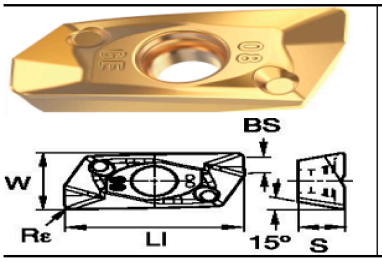

Cutting Tool	
Material Number	6.172.192
ISO Catalog ID	EDPT140408PDSRGE
Grade	KCSM40
Insert Length (LI)	17.471 mm
Insert Cutting Edge Length	17.437 mm
Insert Thickness (S)	4.446 mm
Insert Width (W)	8.17 mm
Corner Facet Length (BS)	2.39 mm
Corner Radius (Rε)	0.8 mm
Tool Holder	
Material Number	2.478.640
ISO Catalog ID	25A03R044B25SED14
Effective Cutting Diameter (D1)	25 mm
Adapter/Shank/Bore Diameter (D)	25 mm
Overall Length (L)	101 mm
Head Length (L2)	44 mm

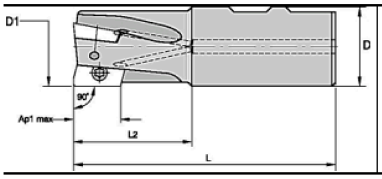

Figure 1. Technical specifications and images of the cutting tool and tool holder.

2.2. MQL Cooling/Lubrication Conditions and Cutting Parameters

In minimum quantity lubrication (MQL), the coolant is delivered to the cutting zone as an atomized mist through a pressurized nozzle. Mackerel Ms MQL fluid, a bio-stable semi-synthetic metalworking fluid with a temperature of 15 °C, a density of 0.90 g/cm^3, and a pH value of 9.5, was used as the coolant. The fluid was supplied to the cutting zone using an SKF UFB20-Basic (AB SKF, Gothenburg, Sweden) MQL system. During the experiments, the coolant was delivered through a nozzle with a diameter of 2 mm at a flow rate of 200 mL/h and a pressure of 4 bar. The nozzle was positioned at an angle of 30° relative to the machining plane and at a distance of 35 mm from the cutting zone, and its position was kept constant throughout the tests. The cutting parameters were selected based on the manufacturer's recommendations and previous studies reported in the literature. In addition, preliminary experiments were conducted within the selected parameter ranges to determine the final parameter levels used in the milling tests. The corresponding cutting parameters and their levels are presented in Table 2.

Table 2. Cutting parameters and levels.

Cutting Parameters	Units	Levels		
		Level 1	Level 2	Level 3
Cooling/Lubrication conditions	-	Dry	MQL	-
Cutting speed, Vc	m/min	30	60	90
Feed rate, f	mm/tooth	0.05	0.09	0.13
Depth of cutting, ap	mm	1	-	-

2.3. Experimental Measurements

Forged, SLM, and post-SLM heat-treated specimens were prepared according to conventional metallographic specimen preparation procedures for microstructural examination and hardness measurements. The specimens were etched with a 3-part Hydrochloric Acid (HCl) and 1-part Nitric Acid (HNO_3) etching solution. A Nikon Eclipse MA200 (Nikon Corporation, Shinagawa-ku, Japan) optical microscope and a Carl Zeiss Ultra Plus Gemini

(ZEISS, Oberkochen, Germany) scanning electron microscope (SEM) were used for microstructural characterization of the specimens. Mechanical tests were performed using a DuraScan-50 G5 (EMCO-TEST, Salzburg, Austria) fully automatic hardness tester to determine the hardness values of the experimental specimens. In addition, the effect of the production processes on porosity was evaluated by density measurements using a Weightlab Instruments WSA-224 (Weightlab Instruments, İstanbul, Turkey) analytical balance based on the Archimedes principle. The experimental setup prepared for the examination of microstructure and mechanical properties is shown in Figure 2.

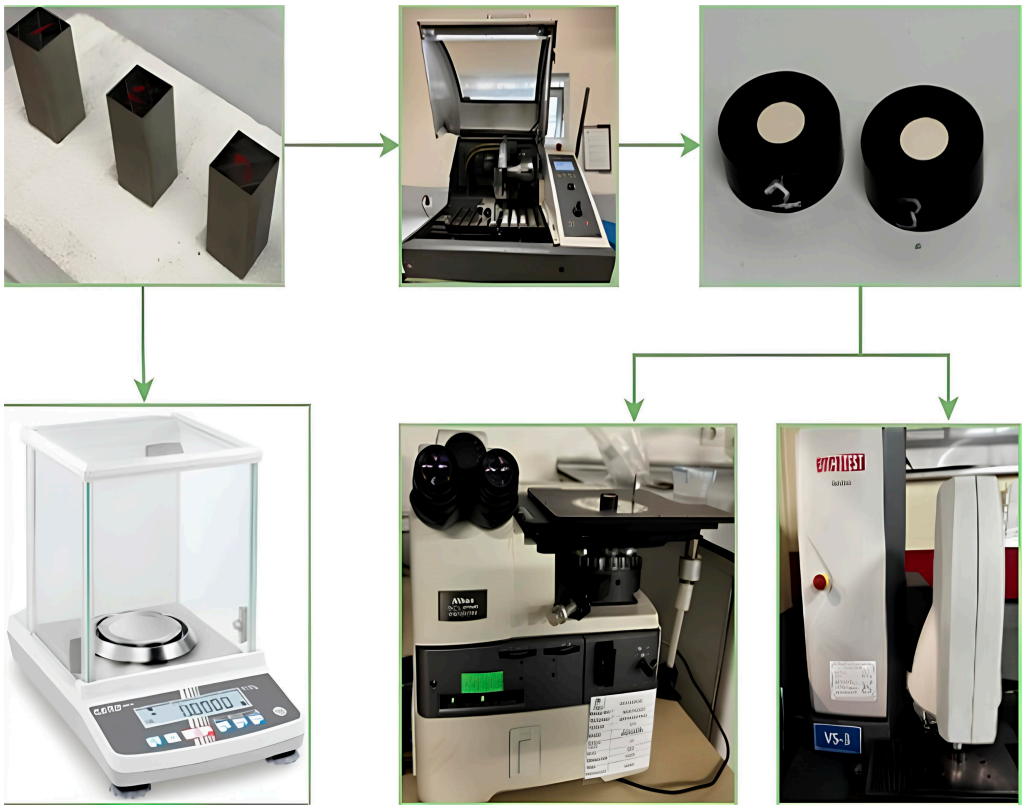

Figure 2. Experimental setup for microstructural and mechanical characterization.

A series of tests were conducted to evaluate the machinability performance of the samples. In milling tests, cutting forces generated depending on microstructure, mechanical properties, machining conditions, and cutting parameters were measured using a KISTLER 9272 A (Kistler Instrumente, Winterthur, Switzerland) type three-axis dynamometer. During machining tests, the signals from the dynamometer were transmitted at appropriate levels to the KISTLER PCIM DAS 1602/16 data acquisition card via a KISTLER 5070-A (Kistler Instrumente, Winterthur, Switzerland) multi-channel amplifier. The obtained data were transferred to the KISTLER Dynoware 2825A-02-01 (Kistler Instrumente, Winterthur, Switzerland) software (Dynoware.exe Version 2.4.1.3) for data analysis. After milling tests, the surface roughness values (Ra) of the workpieces were measured using a MarSurf SW PS1 (Mahr GmbH, Göttingen, Germany) surface roughness measuring device. Four measurements were taken at a 90° angle to the machining direction, and the arithmetic mean of these measurements was calculated to determine the average surface roughness values (Ra). Temperatures generated in the cutting zone during machining tests were measured simultaneously using a FLIR T440 (FLIR Systems, Wilsonville, OR, USA) thermal camera. During the tests, the thermal camera was positioned 450 mm away from the cutting zone at a 45° angle. An Insize ISM-PM200SA (INSIZE Co., Ltd., Suzhou, China) digital microscope with a resolution of 1600 × 1200 was used to determine tool wear. The maximum flank

wear (Vb) was measured as 0.3 mm. A Carl Zeiss Ultra Plus Gemini (ZEISS, Oberkochen, Germany) scanning electron microscope (SEM) was used to provide high-resolution imaging for the analysis of tool wear mechanisms. A schematic overview of the experimental setup for the machinability study is given in Figure 3.

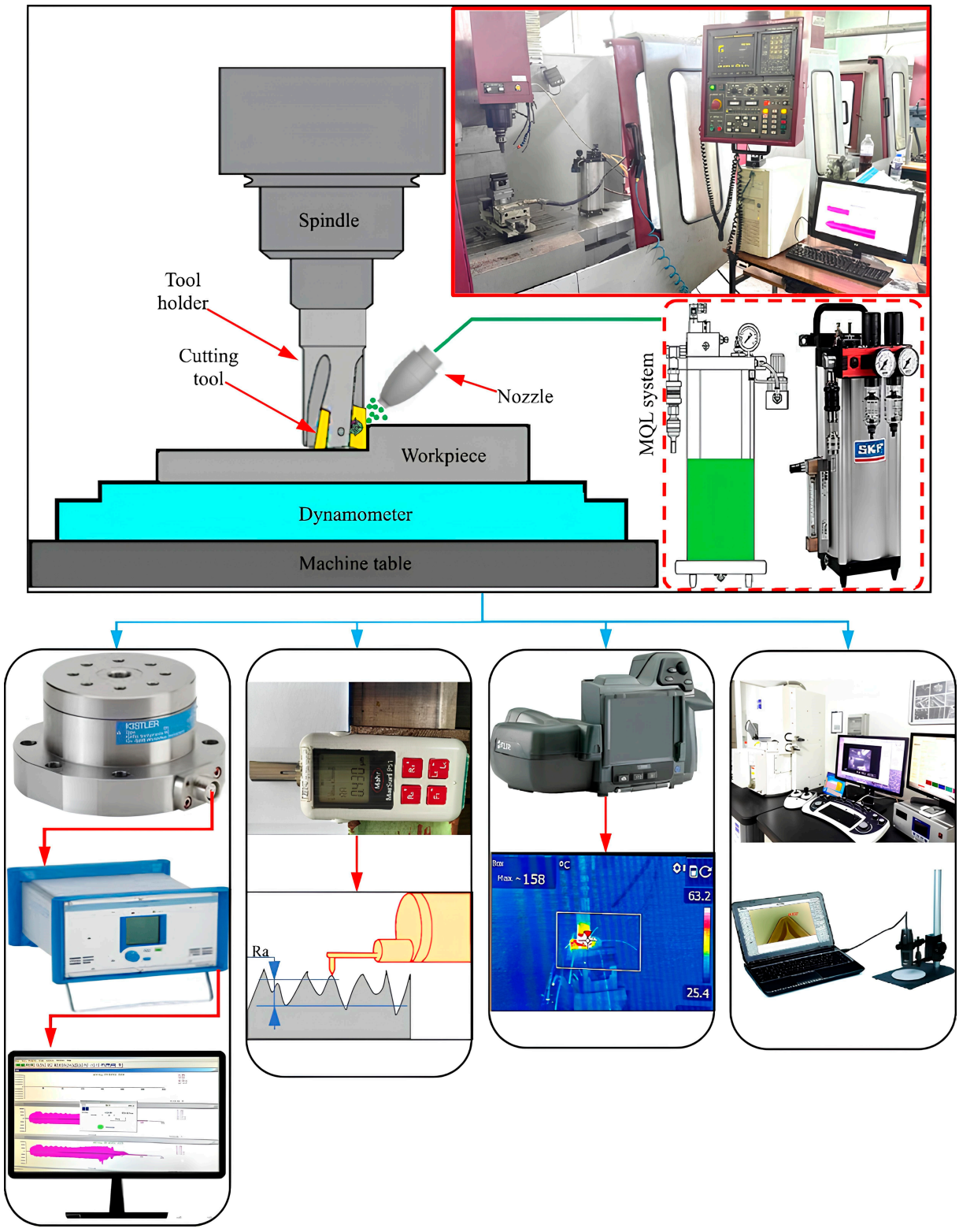

Figure 3. Schematic representation of the experimental setup for the machinability study.

3. Prediction Models

3.1. Linear Regression (LR)

Linear Regression (LR) is a supervised machine learning technique used to model the linear relationship between input and output variables. The method determines the optimal regression coefficients by minimizing the sum of squared errors between observed and predicted values. Owing to its simplicity, interpretability, and low computational cost, LR is widely used in engineering applications for predicting machining responses such as cutting force, surface roughness, cutting temperature, and tool wear. A general representation of the LR model is shown in Figure 4 [32,33].

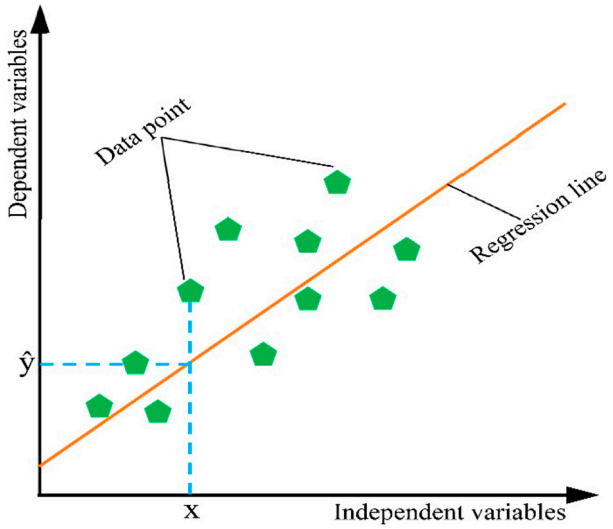

Figure 4. A generalized linear regression model.

3.2. Decision Tree Regression (DTR)

Decision Tree Regression (DTR) is a supervised machine learning technique that predicts output responses based on input variables through a hierarchical tree structure. Owing to its simplicity and interpretability, DTR is widely used in engineering applications for modeling nonlinear relationships. The algorithm recursively partitions the dataset into homogeneous subsets according to decision rules derived from the input variables. The predictive performance of the model depends on the quality and quantity of the training data. A general representation of the DTR model is shown in Figure 5 [34,35].

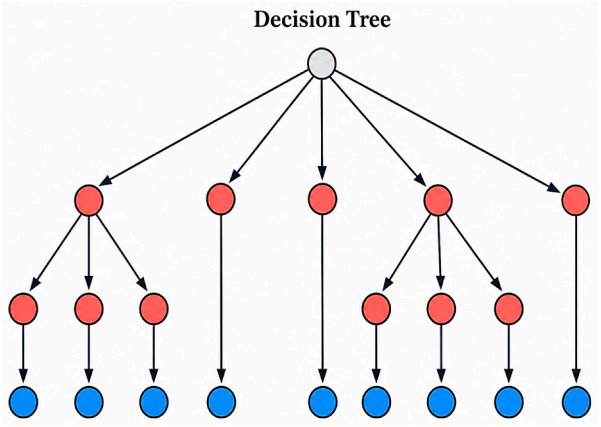

Figure 5. A generalized decision tree regression model.

3.3. Support Vector Regression (SVR)

Support Vector Regression (SVR) is a supervised machine learning method used to model the relationship between input variables and continuous output responses. The method is based on statistical learning theory and aims to construct an optimal hyperplane that fits the data within a specified error margin while maximizing generalization performance. The training data points that define the regression function are referred to as support vectors and play a key role in model formation. Owing to its strong generalization capability, SVR is widely used for modeling complex and nonlinear relationships in engineering applications. In addition, it performs effectively in high-dimensional spaces and provides robust predictions through the use of kernel functions [36,37]. A general representation of the SVR model is shown in Figure 6.

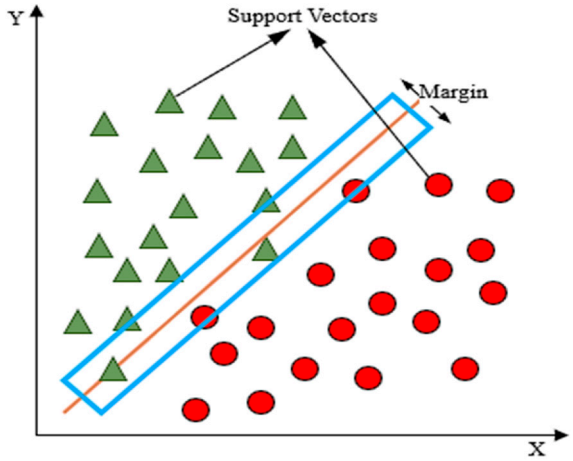

Figure 6. A generalized support vector machines model.

3.4. Gaussian Process Regression

Gaussian Process Regression (GPR) is a probabilistic, non-parametric machine learning method based on Bayesian theory and widely used for regression problems. The method models the target variable as a Gaussian process, providing both predictive mean values and associated uncertainty estimates. This capability is particularly advantageous in engineering applications where prediction confidence is important. GPR is effective in modeling complex and nonlinear relationships between input and output variables. During training, the hyperparameters of the covariance (kernel) function are optimized to capture the underlying data structure, enabling high prediction accuracy, especially for small datasets [38–40]. A general representation of the GPR model is shown in Figure 7.

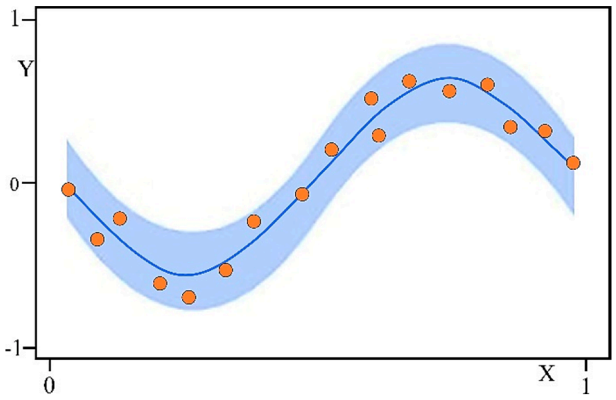

Figure 7. A generalized gaussian process regression model.

3.5. Comparison of Prediction Models

In milling operations, output responses such as cutting force, surface roughness, cutting temperature, and tool wear have a direct influence on product quality and production cost. Therefore, accurate prediction and optimization of both input and output parameters are essential. In this study, machine learning models including Linear Regression (LR), Decision Tree Regression (DTR), Support Vector Regression (SVR), and Gaussian Process Regression (GPR) were employed to predict machining responses. The input parameters considered include manufacturing method, cooling/lubrication condition, cutting speed, and feed rate. The performance of the developed models was evaluated by comparing experimental and predicted values using Equation (1).

$$Accuracy = {}^{1}/_{n}\sum_{n=1}^{n}\left[1 - \frac{|Exp.(i) - Est.(i)|}{Exp.(i)}\right] \times 100 \quad (1)$$

In addition, model performance was assessed using statistical indicators including Mean Absolute Percentage Error (MAPE), Mean Absolute Error (MAE), Root Mean Square Error (RMSE), and Coefficient of Determination (R^2), as given in Equations (2)–(5):

$$MAPE = {}^{1}/_{n}\sum_{i=1}^{n}\frac{\left|Exp.y_i - Est.\hat{y}_i\right|}{Exp.y_i} \quad (2)$$

$$MAE = {}^{1}/_{n}\sum_{i=1}^{n}\left|Exp.y_i - Est.\hat{y}_i\right| \quad (3)$$

$$\mathrm{RMSE} = \sqrt{{}^{1}/_{n}\sum_{i=1}^{n}(\mathrm{Exp.y_i} - \mathrm{Est.\hat{y}_i})^2} \quad (4)$$

$$R^2 = 1 - \frac{\sum_{i=1}^{n}\left(Exp.y_i - \widehat{\mathrm{Est.y}_i}\right)}{\sum_{i=1}^{n}(Exp.y_i - Avg.\ of\ Exp.)} \quad (5)$$

where MAPE, MAE, RMSE, and R^2 denote Mean Absolute Percentage Error, Mean Absolute Error, Root Mean Square Error, and Coefficient of Determination, respectively.

4. Results

4.1. Evaluation of Microstructure and Mechanical Properties

In this study, the changes in microstructure, hardness, and density of commercially produced Inconel 718 (WP1) by forging, and SLM-produced (WP2) and heat-treated SLM (WP3) samples were evaluated. The microstructural images presented in Figures 8–10 clearly demonstrate that both the manufacturing route and subsequent heat treatment significantly influence the microstructure and mechanical properties of the samples. Figure 8 shows the optical microscope and SEM images of the forged WP1 sample, together with EDS results. The microstructure of WP1 exhibits a homogeneous, isotropic, and fine-grained structure. The plastic deformation and thermomechanical history associated with forging are responsible for grain refinement and microstructural homogeneity. This refined microstructure promotes precipitation hardening by increasing dislocation density, resulting in higher hardness. In nickel-based superalloys such as Inconel 718, fine-grained structures facilitate the uniform precipitation of γ'' (Ni_3Nb) and γ' ($Ni_3(Al, Ti)$) phases within the γ matrix [41–44]. This is also supported by the EDS results in Figure 8.

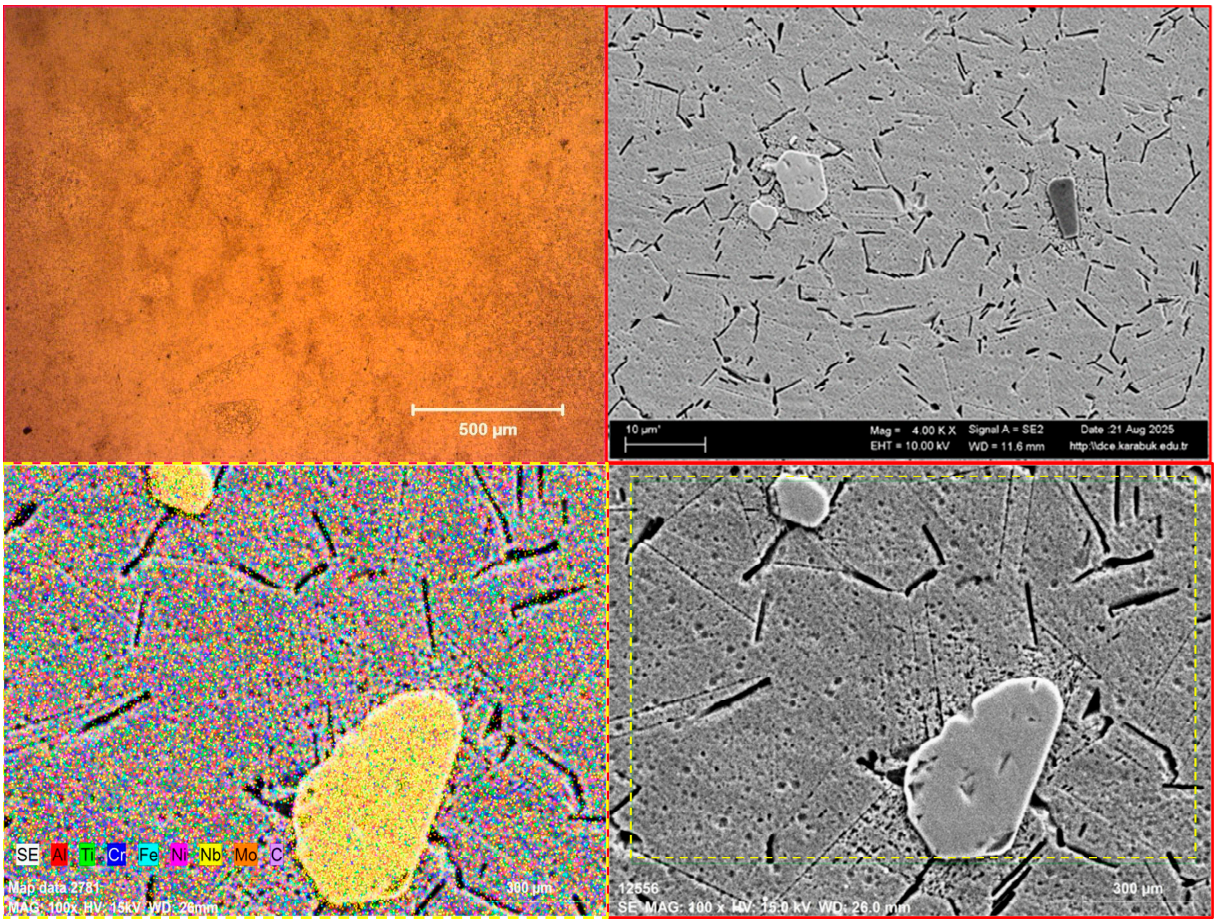

Figure 8. Microstructure, SEM images, and EDS analysis of the WP1 specimen.

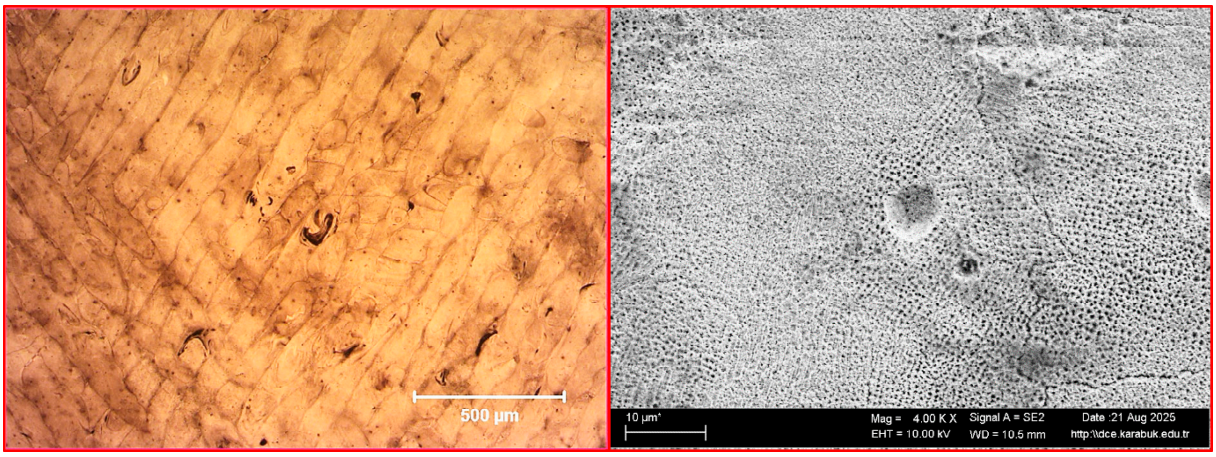

Figure 9. Microstructure and SEM images of the WP2 specimen.

Optical and SEM images of the WP2 sample (Figure 9) reveal a cellular and dendritic microstructure with distinct melt pool boundaries typical of SLM processing. Crack and pore formations were observed on the surface. These defects are attributed to the steep thermal gradients and rapid solidification inherent to the SLM process. The dendritic structure promotes the segregation of alloying elements such as Nb and Mo at cell boundaries, which may lead to Laves phase formation under certain conditions and deteriorate mechanical properties [45–48].

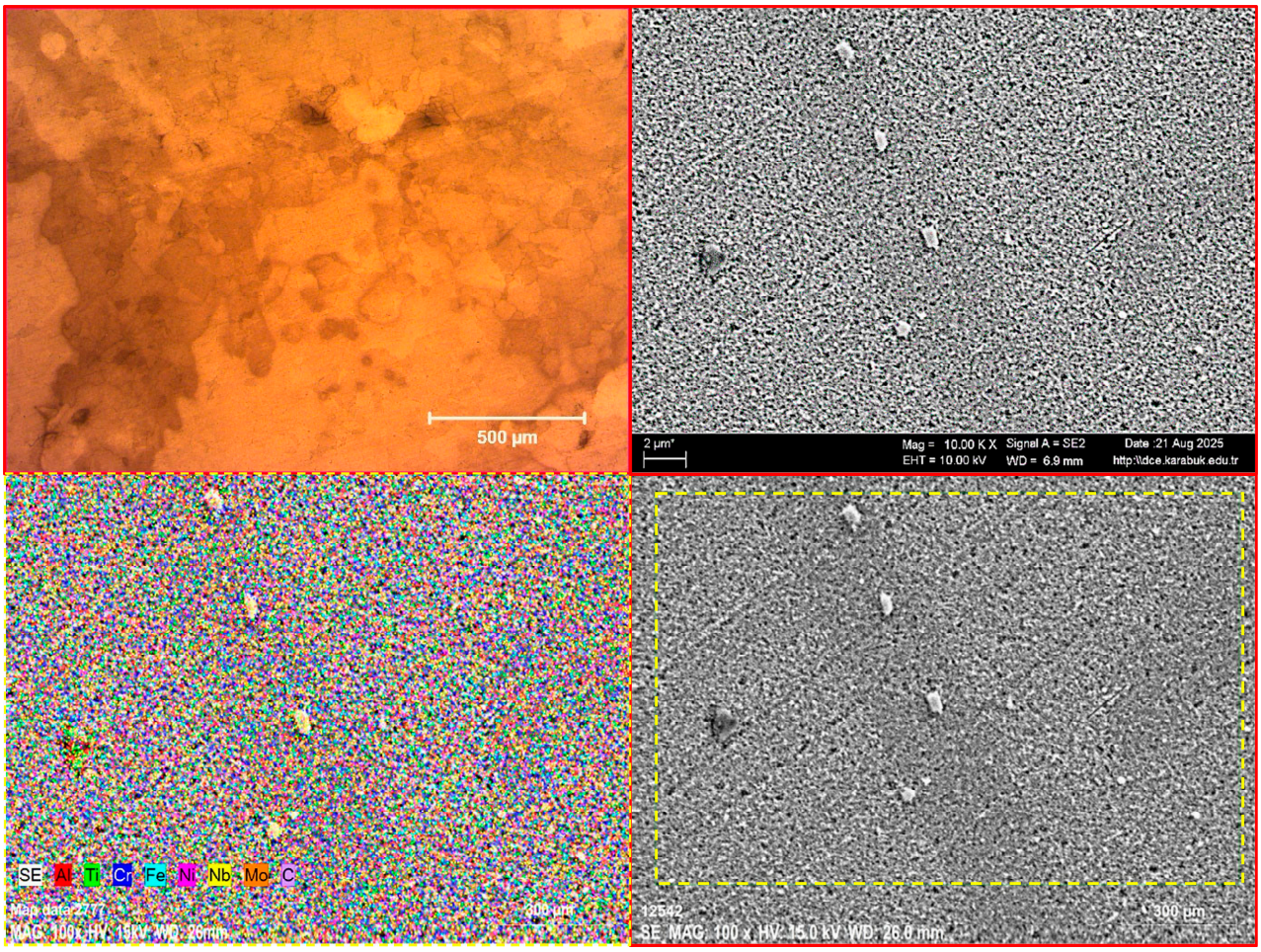

Figure 10. Microstructure, SEM images, and EDS analysis of the WP3 specimen.

Figure 10 presents the optical microscope and SEM images of the WP3 sample, which was subjected to homogenization and aging after SLM. Compared with WP2, WP3 shows a more homogeneous microstructure with reduced segregation and improved elemental distribution. The more uniform distribution of γ' and γ'' precipitates is a key factor enhancing microstructural stability. EDS results indicate local enrichments of Ni and Nb, suggesting Nb-rich regions associated with γ'' precipitation. These features may also be linked to the partial dissolution of Laves phases formed during SLM [42,44,46–48].

Density measurements based on Archimedes' principle were used to evaluate porosity, and the results are shown in Figure 11. WP1 exhibited a relative density of 99.886%, indicating near-full densification and minimal defects. In contrast, WP2 showed a relative density of 97.912%, corresponding to a decrease of approximately 1.98% compared to WP1. This reduction is mainly attributed to porosity and solidification defects typical of SLM. WP3 exhibited an improved relative density of 98.307%, representing an increase of about 0.40% compared to WP2. This improvement is associated with partial pore closure and spheroidization driven by diffusion during heat treatment.

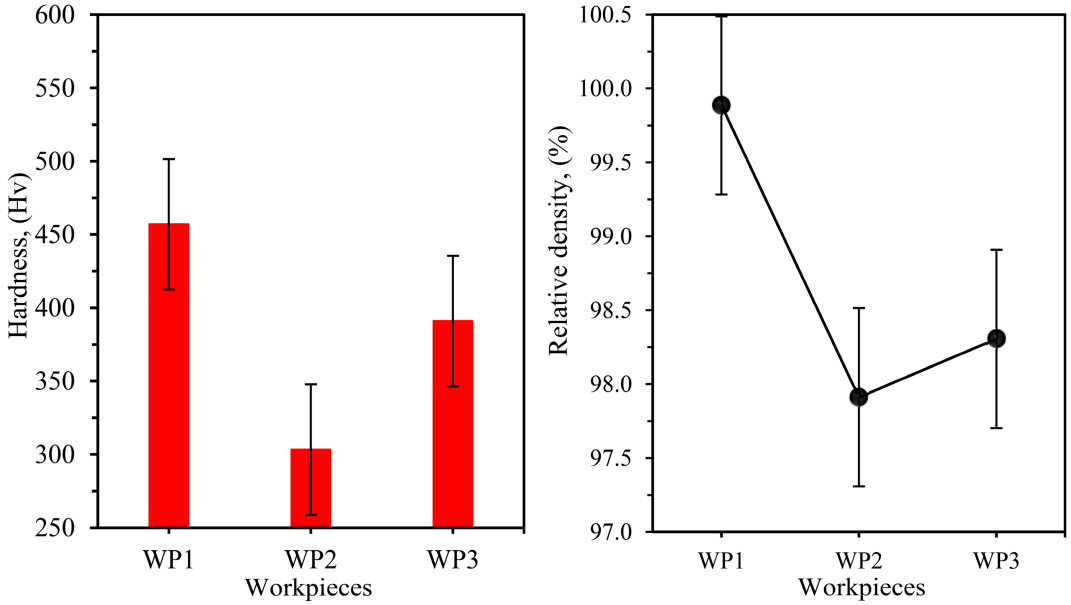

Figure 11. Comparison of hardness and relative density values of the experimental specimens.

Density measurements of the samples were performed based on Archimedes' principle to determine the effect of the manufacturing processes and heat treatment on porosity, and the results are presented in Figure 11. The relative density of sample WP1 was measured as 99.886%. This value indicates that the forging method provides a structure with near-full density and low defects. In contrast, the relative density of sample WP2 was measured to be 97.912%, which corresponds to a decrease of approximately 1.98% compared to sample WP1. This reduction can be explained by the presence of porosity and solidification-related defects associated with the SLM process. In sample WP3, the relative density was measured at 98.307%, representing an improvement of approximately 0.40% compared to that of WP2. This increase can be attributed to the partial closure and spheroidization of pores promoted by diffusion mechanisms during heat treatment.

The hardness results of WP1, WP2, and WP3 are also presented in Figure 11. A similar trend was observed between hardness and relative density. WP1 showed the highest hardness value of 457 HV. In WP2, the hardness decreased to 303.33 HV, corresponding to a reduction of approximately 33.6% compared to WP1. This decrease is attributed to microstructural heterogeneity and the presence of porosity, which facilitates dislocation motion. In contrast, WP3 exhibited an increased hardness of 391 HV, representing an improvement of approximately 28.9% compared to WP2. This increase is explained by the precipitation strengthening effect of γ' and γ'' phases formed during aging. However, WP3 did not reach the hardness level of WP1 due to the incomplete elimination of SLM-induced defects.

4.2. Evaluation of Cutting Force

In milling operations, cutting force is a key response parameter that reflects the interaction between the tool and workpiece under different microstructural conditions, machining environments, and cutting parameters. It is therefore widely used as a primary indicator for evaluating machining performance. In this study, the effects of machining conditions and cutting parameters on cutting forces during milling of Inconel 718 with different microstructures were investigated, and the results are presented in Figure 12.

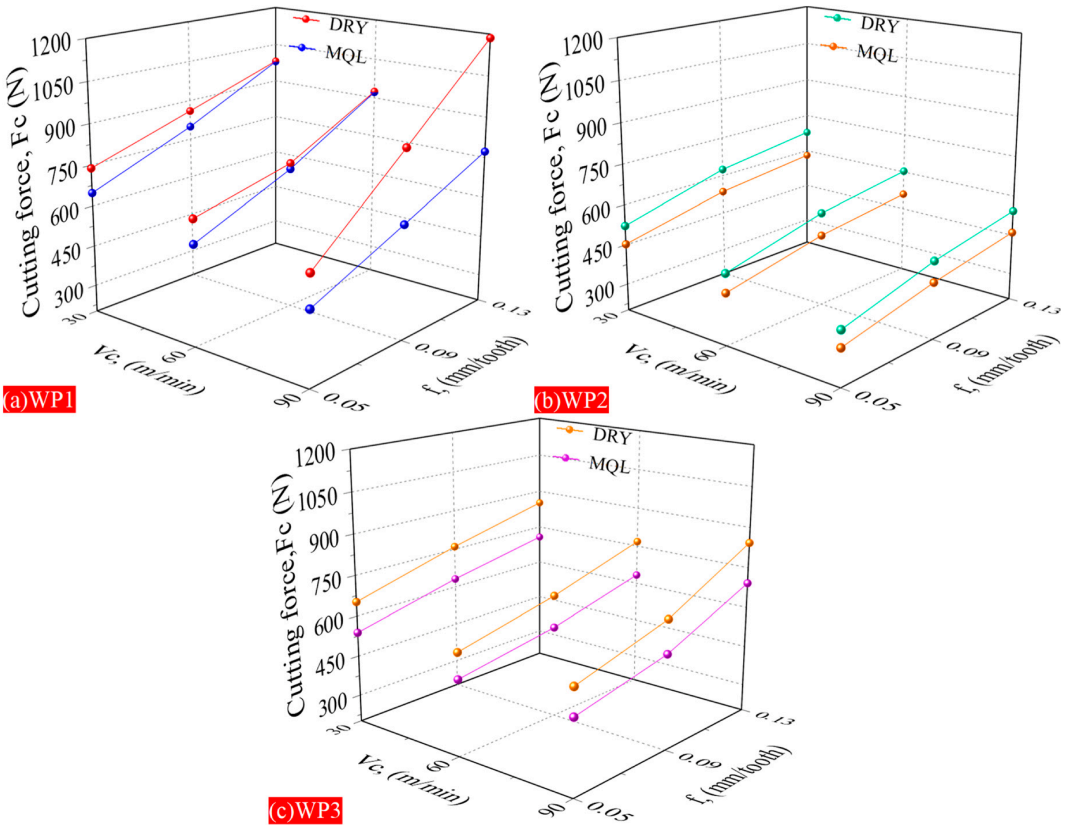

Figure 12. Effects of microstructure, mechanical properties, machining environment, and cutting parameters on cutting forces during the milling of Inconel 718 alloy.

When Figure 12 is examined, it is seen that the cutting force values in the milling tests varied between 336.5 and 1185.9 N. The minimum cutting force was measured as 336.5 N when the WP2 specimen, produced by SLM, was machined under MQL machining conditions at a cutting speed of 90 m/min and a feed rate of 0.05 mm/tooth. The maximum cutting force was 1185.9 N when the WP1 specimen, produced by forging, was milled under dry machining conditions at a cutting speed of 90 m/min and a feed rate of 0.13 mm/tooth. When Figure 12 is examined, it is observed that the cutting forces generally decrease with increasing cutting speed. This result is consistent with previous studies in the literature [49,50]. For example, Thakur et al. reported that the cutting force decreased with increasing cutting speed when machining Inconel 718 [51]. Hao et al. showed that when other cutting parameters were kept constant during Inconel 718 milling, the cutting force also decreased with increasing cutting speed [52]. It was observed that increasing the feed rate caused a significant increase in cutting force values. These data were also confirmed by Gupta et al. [53]. Similarly, Bai et al. reported that cutting forces increased with increasing feed rates when machining Inconel 625 and Inconel 718 [54]. Furthermore, the study conducted by Çakıroğlu also stated that increasing the feed rate increased cutting forces during the machining of Inconel 718 [55].

Experiments conducted on samples under MQL machining conditions at a constant cutting speed and feed rate show that the cutting force values obtained are, on average, 15.5% lower compared to dry machining conditions. This can be explained by the improvement of tribological and thermal conditions in the cutting zone during the milling process. The MQL application significantly reduces the friction coefficient at tool/chip and tool/workpiece interfaces by providing a thin oil film to the cutting zone. This directly contributes to the reduction in cutting forces. This situation is consistent with previous studies in the literature [56,57]. In addition, the partial cooling and effective lubrication

effect provided by MQL limits the temperature generated in the cutting zone, reducing the tendency to stick and the formation of build-up chips (BUE). Suppressing build-up chips allows the cutting edge to operate more stably and efficiently, thus reducing the deformation resistance during cutting. Furthermore, under lower temperature and friction conditions, the chip flow becomes more regular, and the energy required for plastic deformation decreases, resulting in a reduction in total cutting forces [58,59].

The influence of microstructure and mechanical properties on cutting forces was also evaluated. The average cutting force for the WP1 sample was 781.28 N. Compared to WP1, the WP2 sample showed a reduction of approximately 39.1%. In contrast, WP3 exhibited an increase of 22.4% compared to WP2. The higher cutting forces in WP1 are attributed to its fine-grained and homogeneous microstructure, which increases dislocation density and resistance to plastic deformation. The lower forces observed in WP2 are associated with its dendritic structure, microstructural anisotropy, and higher porosity, which reduce deformation resistance. Although heat treatment improved the mechanical strength of WP3 through precipitation hardening, partial elimination of SLM-induced porosity and defects resulted in intermediate cutting force levels between WP1 and WP2.

4.3. Evaluation of Surface Roughness

Surface roughness (Ra) is a key indicator of surface integrity in materials with different microstructures and mechanical properties machined under dry and MQL conditions. It is widely used to evaluate surface quality and machinability performance. In this study, the effect of machining conditions and cutting parameters on surface roughness during milling of Inconel 718 was investigated, and the results are presented in Figure 13.

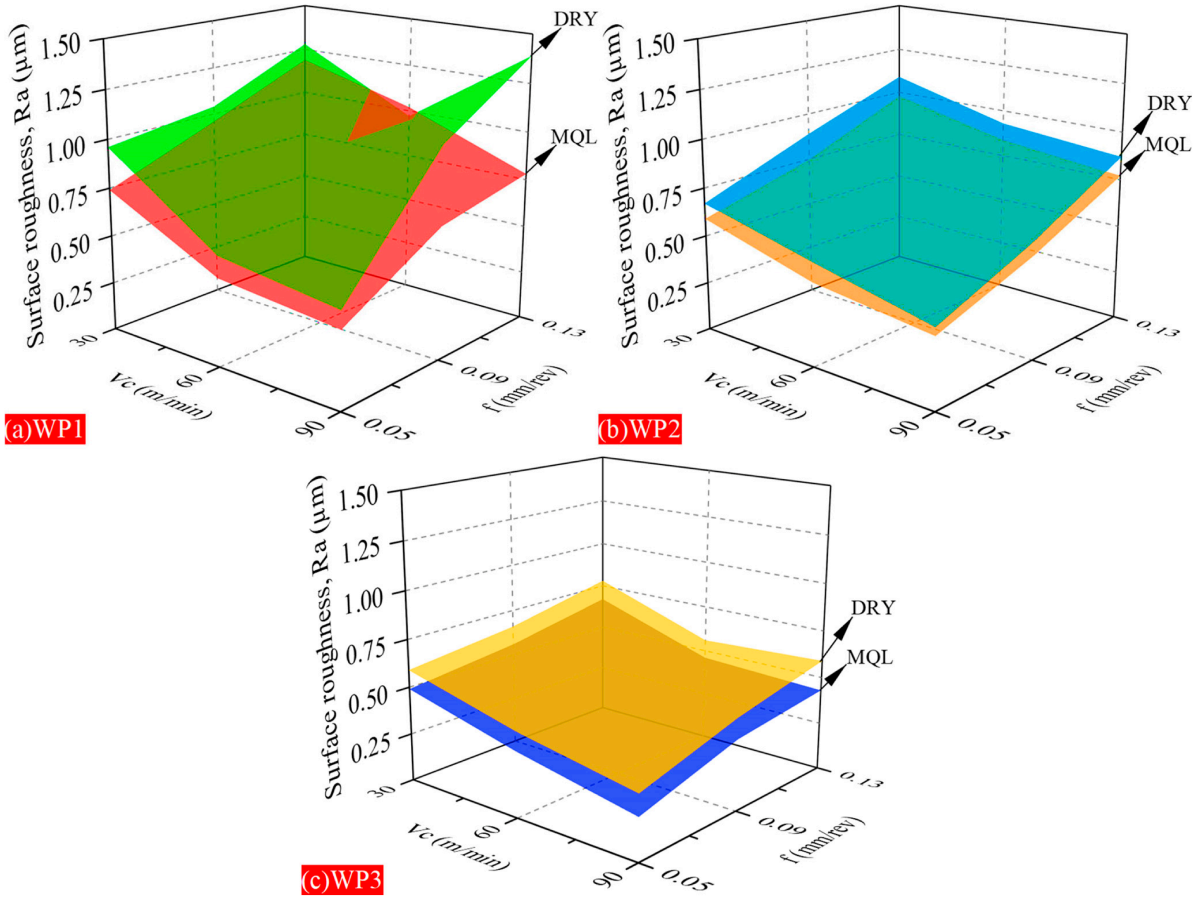

Figure 13. Effects of microstructure, mechanical properties, machining environment, and cutting parameters on surface roughness during the milling of Inconel 718 alloy.

Figure 13 shows that the surface roughness values in the milling tests varied between 0.22 µm and 1.39 µm. In this study, the minimum surface roughness value was obtained for sample WP3 under MQL machining conditions at a cutting speed of 90 m/min and a feed rate of 0.05 mm/tooth (0.22 µm). In contrast, the maximum surface roughness value was measured for sample WP1 under dry machining conditions at a cutting speed of 90 m/min and a feed rate of 0.13 mm/tooth (1.39 µm). Examining Figure 13, it is generally observed that the surface roughness values decrease with increasing cutting speed. This can be explained by the reduction in friction at the tool/workpiece interface at high cutting speeds, the more stable chip formation mechanism, and the reduction in embedded chip formation. The results obtained are consistent with studies reported in the literature [60–62]. For example, Kawasaki et al. reported that increasing the cutting speed resulted in lower surface roughness values when milling Inconel 718 [63]. Similarly, in the study conducted by Wu and Lin, it was stated that high cutting speeds improved surface quality and contributed to obtaining lower Ra values when milling Inconel 718 [64].

Machining the test specimens under MQL conditions with constant cutting speed and feed rate resulted in lower surface roughness values compared to dry machining conditions. This can be attributed to the fact that MQL application improves the tribological conditions in the cutting zone, reducing friction and thermal loads at the tool/workpiece interface. In machinability tests, the controlled delivery of oil droplets made the chip formation mechanism more stable, while contributing to the reduction in plastic deformation marks, irregular tool marks, and adhesion-related defects on the surface. Furthermore, MQL application has supported the preservation of surface integrity by limiting negative effects such as chip accumulation and tool adhesion [65–68]. The literature also reports that MQL application improves surface quality and provides lower surface roughness values in the machining of Inconel 718 alloy. For example, in the study conducted by De Bartolomeis et al., it was stated that the electrostatically assisted MQL (EMQL) system used in high-speed milling of Inconel 718 improved surface roughness by reducing tool wear [69]. Similarly, in the study evaluating sustainable machining strategies, it was stated that MQL and hybrid nanofluid-MQL applications provided lower surface roughness values compared to dry machining, and this was associated with increased lubrication performance in the cutting zone [70].

Surface roughness also varied significantly depending on the microstructure and mechanical properties of the workpieces. WP1 exhibited higher Ra values due to its high hardness and resistance to plastic deformation, which increase cutting forces and surface damage. WP2 showed lower hardness and density due to its dendritic structure, anisotropy, and porosity, which reduced cutting resistance but introduced surface irregularities. WP3 exhibited improved surface quality compared to WP2 due to homogenization and aging treatment, which reduced segregation and promoted a more stable γ'/γ'' precipitate distribution, leading to improved chip formation and surface integrity.

4.4. Evaluation of Cutting Temperature

During machining of materials with different microstructures under dry and MQL conditions, cutting temperature is a key thermal response reflecting tool–workpiece interaction. It is widely used to evaluate heat generation and thermal behavior in the cutting zone. In this study, the effects of machining conditions and cutting parameters on cutting temperature during milling of Inconel 718 were investigated, and the results are presented in Figure 14.

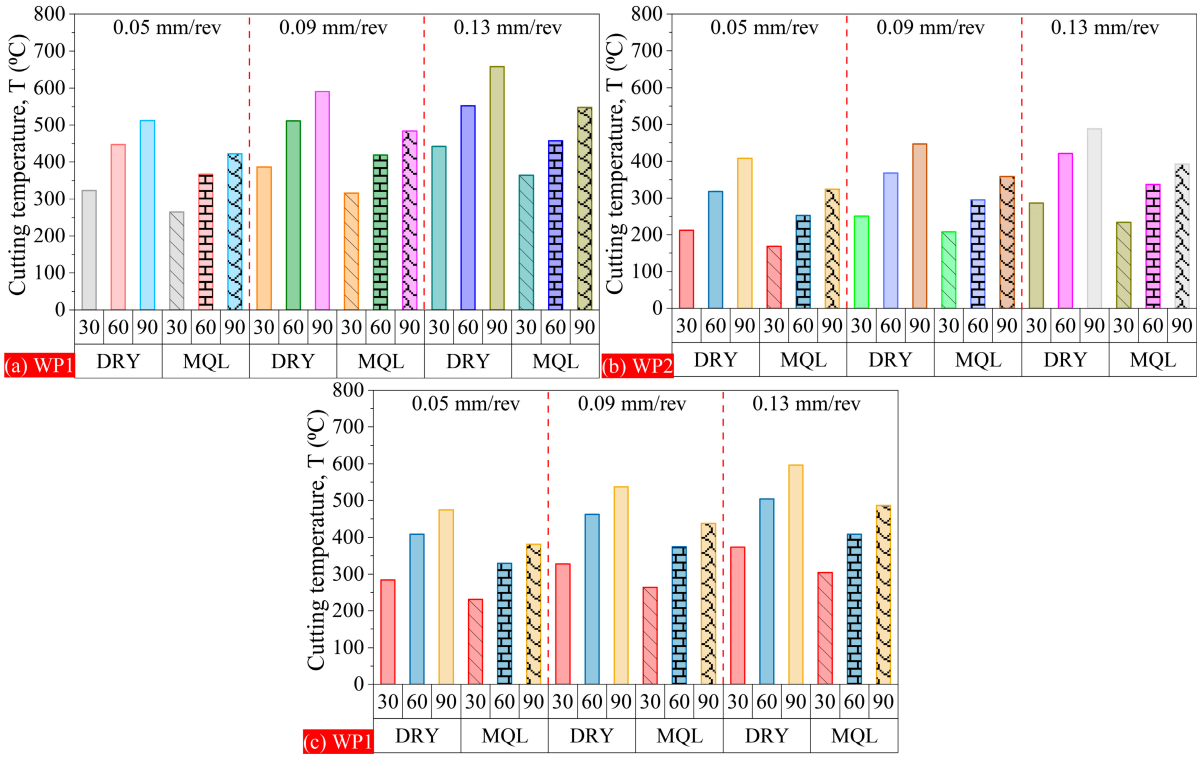

Figure 14. Effects of microstructure, mechanical properties, machining environment, and cutting parameters on cutting temperature during the milling of Inconel 718 alloy.

Figure 14 shows that the cutting temperature values in the milling tests varied between 168–658 °C. The minimum cutting temperature was measured as 168 °C when the WP2 specimen was machined under MQL machining conditions at a cutting speed of 30 m/min and a feed rate of 0.05 mm/tooth. The maximum cutting temperature, on the other hand, increased by approximately 290% to 658 °C when the WP1 specimen was milled under dry machining conditions at a cutting speed of 90 m/min and a feed rate of 0.13 mm/tooth. Figure 14 shows that, in general, the cutting temperature increases with increasing cutting speed and feed rate. Increasing the cutting speed and feed rate causes the cutting temperature to rise due to greater plastic deformation in the cutting zone. The increase in cutting speed leads to a greater energy release per unit time due to friction between the tool and the workpiece. However, despite the increased rate of heat generation, the time it takes for this heat to dissipate to the environment decreases. This situation causes a significant increase in cutting temperature, especially in materials with low thermal conductivity, such as nickel-based superalloys. Increasing the feed rate increases the chip cross-sectional area, thereby increasing cutting forces and plastic deformation, and consequently, friction heat. Therefore, both increased cutting speed and feed rate lead to higher thermal load in the cutting zone and an increase in temperature at the tool/workpiece interface. This situation has been similarly reported in the literature. For example, studies by Zheng et al., Fernandes et al., and Karagöz et al. emphasized that increasing cutting parameters significantly increases the cutting temperature, especially in machining superalloys, and accelerates tool wear [71–73]. Furthermore, numerous studies have indicated that heat accumulation is a critical problem in machining Inconel 718 alloy, which has low thermal conductivity.

Experiments conducted under MQL machining conditions at a constant cutting speed and feed rate show that the cutting temperature values obtained are on average 18.65% lower than those obtained under dry machining conditions. Figure 14 shows that dry and MQL machining conditions create significant differences in heat generation and heat transfer mechanisms in the cutting zone. In dry machining conditions, since there is no

external lubrication and cooling mechanism in the cutting zone, a large portion of the generated plastic deformation energy is converted into heat, and a significant portion of this heat accumulates at the tool/workpiece interface. This situation leads to an increase in cutting temperature, accelerated tool wear, and negatively impacts surface integrity [74]. In contrast, MQL application reduces friction and limits heat generation by delivering micro-level oil particles to the cutting zone. The lubricant film layer reduces heat generation from friction by decreasing the contact area at the tool/chip interface and also facilitates heat dissipation. It has been reported in the literature that MQL significantly reduces cutting temperature and reduces thermal loads, especially in nickel-based superalloys [75].

The influence of microstructure on cutting temperature was also evaluated. The average cutting temperature for WP1 was 448 °C. Compared to WP1, WP2 exhibited a reduction of approximately 28.5%, while WP3 showed an increase of 24.5% relative to WP2. The higher temperature in WP1 is attributed to its fine-grained, dense microstructure, which increases resistance to plastic deformation and thus heat generation. In contrast, WP2 exhibits lower temperatures due to dendritic structure, porosity, and microstructural heterogeneity, which reduce effective shear strength and deformation energy. WP3 shows intermediate thermal behavior due to homogenization and precipitation hardening, which improve structural stability while partially retaining residual defects from the SLM process.

4.5. Evaluation of Tool Wear

Tool wear occurs due to the combined effect of high temperature, friction, adhesion, and mechanical loads in the cutting zone, and is considered a critical machinability indicator, especially when machining superalloys with low thermal conductivity and high work-hardening tendency, such as Inconel 718. In this context, milling of Inconel 718 samples produced by forging (WP1), by SLM (WP2), and by SLM followed by heat treatment (WP3) was performed under DRY and MQL conditions with constant cutting parameters (90 m/min cutting speed, 0.13 mm/tooth feed rate, and 1 mm cutting depth). The results of experiments conducted to determine the effects of machining conditions, microstructure, and mechanical properties on tool wear are presented in Figure 15. Additionally, cutting tool wear images under dry cutting conditions are given in Figure 16, and SEM images under MQL conditions are given in Figure 17.

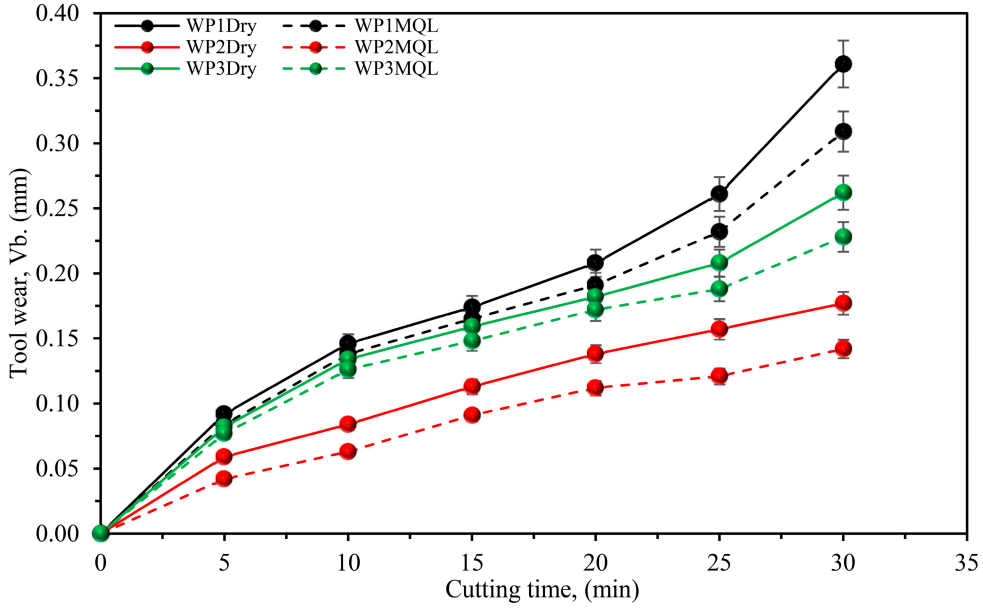

Figure 15. Effects of microstructure, mechanical properties, and cutting conditions on tool wear.

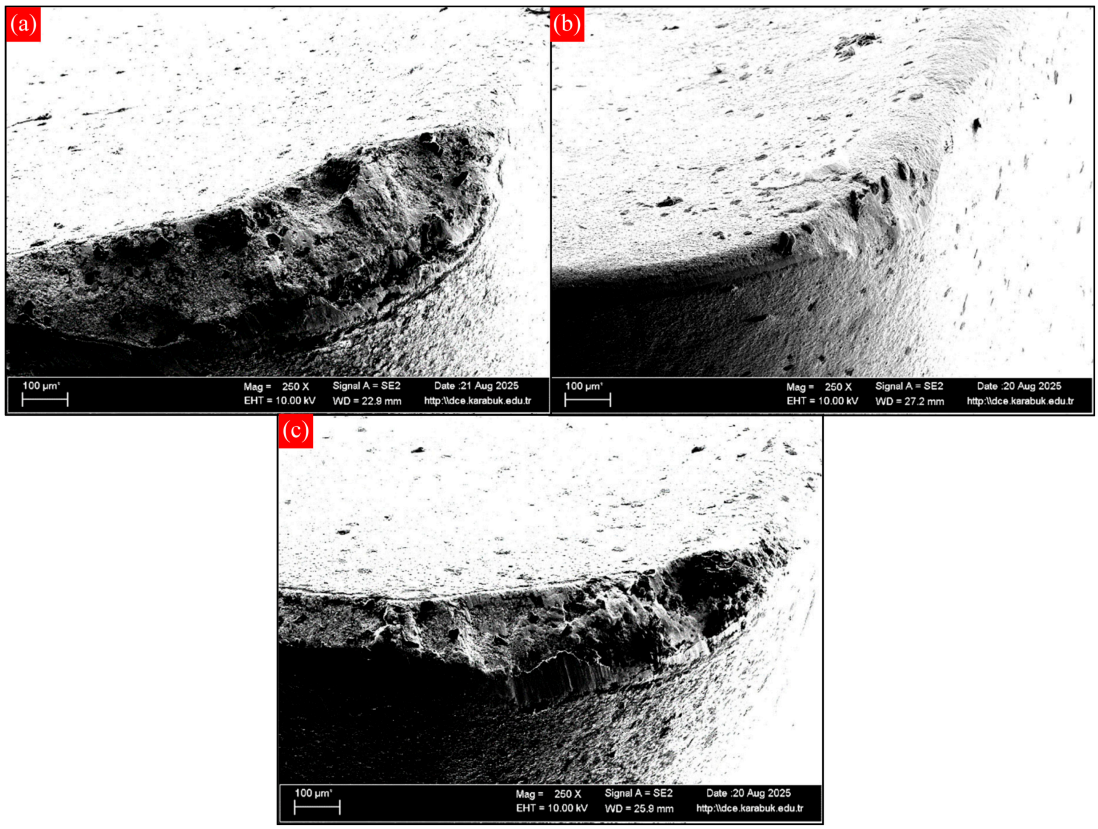

Figure 16. SEM images of cutting tools under dry machining conditions as influenced by the microstructure and mechanical properties of: (**a**) WP1, (**b**) WP2, and (**c**) WP3.

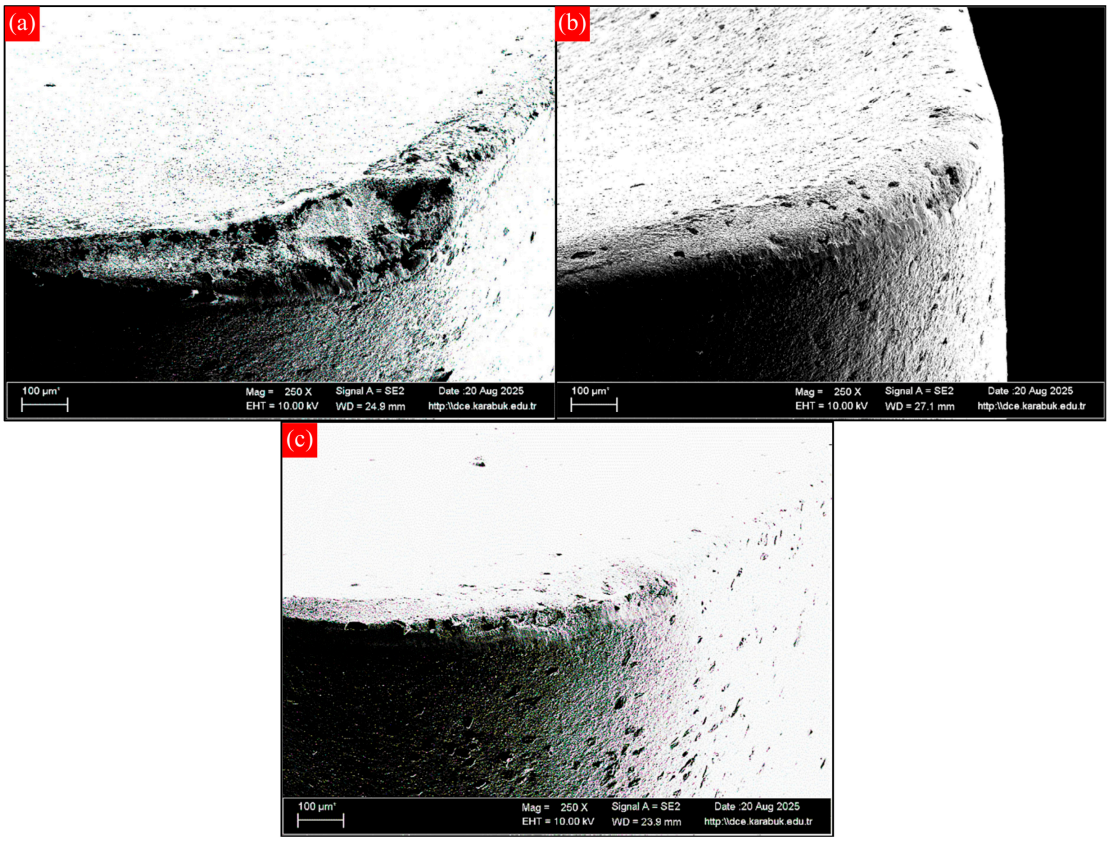

Figure 17. SEM images of cutting tools under MQL machining conditions as influenced by the microstructure and mechanical properties of: (**a**) WP1, (**b**) WP2, and (**c**) WP3.

Figure 15 shows that in all samples, tool wear values under MQL machining conditions are, on average, 15.1% lower compared to dry machining conditions. This can be explained by the fact that MQL application improves the tribological and thermal conditions in the cutting zone. The oil particles delivered to the cutting zone by the MQL system reduce friction at the tool/chip and tool/workpiece interfaces, limiting the tendency for adhesion. In addition, the resulting thin lubricant film partially suppresses the temperature increase in the cutting zone, reducing the effect of diffusion and adhesion-based wear mechanisms. Therefore, it is clearly observed in the SEM images in Figure 17 that under MQL conditions, compared to dry machining conditions, there is less coating damage, more limited abrasive marks, and fewer microfractures on the tool surface. In contrast, under dry machining conditions, due to the absence of any effective lubrication and cooling mechanism in the cutting zone, a large portion of the heat generated accumulates at the tool/chip interface, accelerating tool wear. In particular, the SEM images given in Figure 16 clearly show dense adhesion layers, coating peeling, abrasive wear, and cutting-edge deformations. Generally, when the SEM images given in Figures 16 and 17 are examined, it is determined that the dominant wear mechanisms under dry machining conditions are adhesion, abrasive, and diffusion wear, as well as coating peeling; while under MQL conditions, the severity of these mechanisms is significantly reduced due to the decrease in friction and cutting temperature.

When evaluated in terms of microstructure and mechanical properties, it was determined that the highest tool wear occurred during the machining of the WP1 sample produced by the forging method. The fine-grained, homogeneous, and high-density microstructure of the WP1 sample, along with its high hardness of 457 HV, increased the mechanical and thermal loads on the tool during cutting, accelerating abrasive and adhesion-diffusion wear mechanisms. Due to its high deformation resistance, friction and heat generation at the tool/chip interface increased, and significant adhesion layers and coating damage were observed in the SEM images. In contrast, the lowest tool wear was obtained in the WP2 sample produced by the SLM method. WP2's oriented dendritic microstructure, microstructural heterogeneity, porosity content, and low hardness of 303.33 HV reduced cutting force and temperature, limiting tool wear. SEM examinations revealed lower adhesion formation and limited abrasive marks, while irregular wear marks due to localized porosity areas were also observed. In the homogenized and aged WP3 sample, tool wear was found to be increased compared to WP2, but remained at a lower level compared to WP1. The more homogeneous distribution of γ' and γ'' precipitates after heat treatment increased the hardness to 391 HV and improved deformation resistance. However, the reduction in segregation areas and the more homogeneous microstructure allowed for more controlled wear; SEM images showed moderate adhesion layers, abrasive scratches, and coating deformations.

4.6. Machine Learning Results

Four different regression-based machine learning approaches (Linear Regression (LR), Decision Tree Regression (DTR), Support Vector Regression (SVR), and Gaussian Process Regression (GPR)) were used to predict the cutting force, surface roughness, and cutting temperature values obtained from milling tests. A total of 54 experimental data points were used in the models developed for each output variable. The dataset was randomly divided into 70% training and 30% testing. Two different cooling/lubrication conditions (dry and MQL), three different workpieces (WP1, WP2, and WP3), three different cutting speeds, and three different feed rates were considered as model inputs. To reduce potential biases that might arise from the different scales and units of the input variables, standard scaling was applied to the training and test data.

To further evaluate the robustness and generalization capability of the developed machine learning models, a 6-fold cross-validation procedure was additionally performed. In this approach, the complete dataset consisting of 54 experimental samples was divided into six approximately equal subsets. For each iteration, five subsets were used for model training and the remaining subset was used for validation. This process was repeated six times until every subset had been used once as the validation dataset. The final model performance was calculated as the average of all folds. The obtained cross-validation results confirmed the reliability of the developed models and reduced the risk of overfitting associated with limited datasets.

The cutting force, surface roughness, and cutting temperature values obtained from the milling tests, as well as the values obtained from the LR, DTR, SVR, and GPR predictions, are shown in Table 3. The comparison of the cutting force, surface roughness, and cutting temperature test results with the predicted values obtained from LR, DTR, SVR, and GPR is shown in Figures 18–20, respectively. Examining Figures 18–20, it is seen that there is a high level of agreement between the experimental results and the predicted values obtained from the LR, DTR, SVR, and GPR models for all output parameters. Furthermore, the accuracy rates of the regression models are presented in detail in Table 4. When the cutting force results given in Figure 18 are evaluated together with the accuracy rates in Table 4, it is determined that the highest performance in predicting the cutting force is obtained by the GPR model with an accuracy rate of 98.7257%. The GPR model was followed by the SVR, DTR, and LR models, respectively. When the surface roughness results presented in Figure 19 and the accuracy values in Table 4 are compared, it is seen that the most successful model in predicting surface roughness is the LR model with an accuracy rate of 94.6299%. The relatively high prediction accuracy of the Linear Regression model for surface roughness can be attributed to the nearly linear relationship between the selected machining parameters and the measured Ra values within the investigated machining window. In particular, the feed rate exhibited a consistent increasing effect on surface roughness, while MQL application produced a nearly uniform reduction in Ra across all workpiece materials. Similarly, the influence of cutting speed showed a gradual decreasing tendency without abrupt nonlinear transitions. Since the experiments were conducted within a relatively narrow and stable range of machining parameters, the surface roughness response remained approximately linear, allowing the LR model to represent the experimental data with high accuracy. In predicting this parameter, the LR model was followed by the SVR, GPR, and DTR models, respectively. When the cutting temperature results given in Figure 20 are examined together with the accuracy rates in Table 4, it is determined that the highest accuracy in predicting the cutting temperature is provided by the GPR model with 98.9967%. In terms of prediction performance for shear temperature, the GPR model was followed by the SVR, DTR, and LR models, respectively. Although the dataset consisted of only 54 experimental observations, the high prediction accuracy achieved by the GPR model can be attributed to the relatively systematic and well-defined relationships between the selected machining parameters and the output responses within the investigated parameter domain. Furthermore, the additional 6-fold cross-validation analysis confirmed the robustness and generalization capability of the developed models, indicating that the obtained prediction performances are not solely a consequence of overfitting. Nevertheless, the authors acknowledge that larger datasets covering wider machining conditions would further improve model robustness and industrial applicability.

Table 3. Experimental results with prediction results obtained using four different regression-based machine learning models.

Exp. No	Exp. Fc (N)	Est. Fc (N)	Exp. Ra (μm)	Est. Ra (μm)	Exp. T (°C)	Est. T (°C)	Exp. Fc (N)	Est. Fc (N)	Exp. Ra (μm)	Est. Ra (μm)	Exp. T (°C)	Est. T (°C)
				Linear Regression						**Decision Tree Regression**		
3	981.7	913.7524	1.28	1.3251	442	409.7963	981.7	960.8500	1.28	1.1117	442	291.0000
5	742.8	753.7221	0.91	0.9444	511	453.6574	742.8	771.1833	0.91	1.1117	511	483.3889
8	885.4	704.9817	1.08	0.8300	591	545.4352	885.4	771.1833	1.08	1.1117	591	483.3889
10	521.4	629.5707	0.67	0.6836	212	289.3796	521.4	426.9333	0.67	0.7400	212	291.0000
15	603.1	803.4098	0.93	0.9375	421	476.9907	603.1	503.9000	0.93	0.9133	421	483.3889
16	397.3	532.0897	0.40	0.4547	407	472.9352	397.3	426.9333	0.40	0.4500	407	483.3889
20	760.2	679.2584	0.66	0.6767	327	312.7130	760.2	649.6833	0.66	0.6250	327	291.0000
22	575.4	519.2281	0.44	0.4601	408	356.5741	575.4	649.6833	0.44	0.3325	408	483.3889
30	979.2	812.1709	1.19	1.2007	364	329.7963	979.2	960.8500	1.19	0.9200	364	291.0000
32	721.4	652.1406	0.89	0.8200	419	373.6574	721.4	771.1833	0.89	0.9200	419	392.8333
35	619.6	603.4001	0.68	0.7056	484	465.4352	619.6	771.1833	0.68	0.9200	484	392.8333
37	452.5	527.9892	0.59	0.5592	168	209.3796	452.5	426.9333	0.59	0.7400	168	291.0000
42	509.3	701.8283	0.84	0.8131	337	396.9907	509.3	503.9000	0.84	0.9133	337	392.8333
43	336.5	430.5082	0.36	0.3303	324	392.9352	336.5	426.9333	0.36	0.4500	324	392.8333
47	631.7	577.6768	0.56	0.5522	264	232.7130	631.7	536.0167	0.56	0.6250	264	291.0000
49	479.6	417.6466	0.34	0.3357	329	276.5741	479.6	536.0167	0.34	0.3325	329	392.8333
				Support vector machines						**Gaussian process regression**		
3	981.7	968.5297	1.28	1.2683	442	427.3212	981.7	972.4145	1.28	1.2597	442	437.3333
5	742.8	762.0582	0.91	0.8927	511	489.3959	742.8	778.1797	0.91	0.9455	511	507.0047
8	885.4	714.9713	1.08	0.7885	591	580.1541	885.4	867.3731	1.08	0.8919	591	589.6105
10	521.4	546.5600	0.67	0.7002	212	222.8762	521.4	537.0248	0.67	0.7049	212	210.1558
15	603.1	697.7737	0.93	0.9234	421	435.0535	603.1	587.4520	0.93	0.9265	421	413.2072
16	397.3	439.7872	0.40	0.4302	407	417.6649	397.3	402.6766	0.40	0.4370	407	397.2747
20	760.2	720.1400	0.66	0.6815	327	318.6014	760.2	757.2251	0.66	0.6685	327	328.7546
22	575.4	581.4838	0.44	0.4084	408	388.4709	575.4	578.7395	0.44	0.3968	408	405.8128
30	979.2	914.0569	1.19	1.1623	364	353.5449	979.2	970.3864	1.19	1.1541	364	363.2142
32	721.4	686.4082	0.89	0.7899	419	406.1978	721.4	724.1639	0.89	0.7943	419	417.2231
35	619.6	610.9019	0.68	0.6781	484	476.3038	619.6	623.1968	0.68	0.6923	484	486.5187
37	452.5	468.6676	0.59	0.6157	168	177.974	452.5	456.0033	0.59	0.6154	168	167.2806
42	509.3	594.6825	0.84	0.8094	337	347.7272	509.3	513.9959	0.84	0.7902	337	330.5648
43	336.5	346.9321	0.36	0.3304	324	323.3381	336.5	336.7949	0.36	0.3186	324	316.0373
47	631.7	607.1812	0.56	0.5857	264	264.1445	631.7	625.4381	0.56	0.5868	264	268.1477
49	479.6	482.7287	0.34	0.3159	329	318.1541	479.6	479.1775	0.34	0.3180	329	328.1131

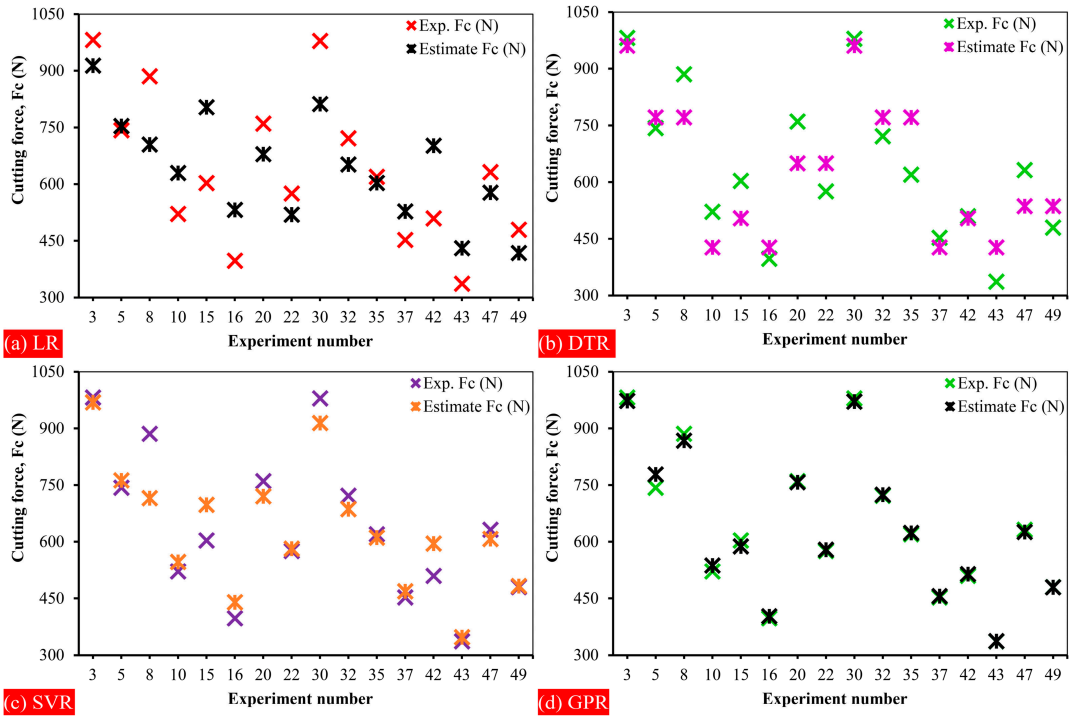

Figure 18. Comparison of experimental and predicted results for cutting force.

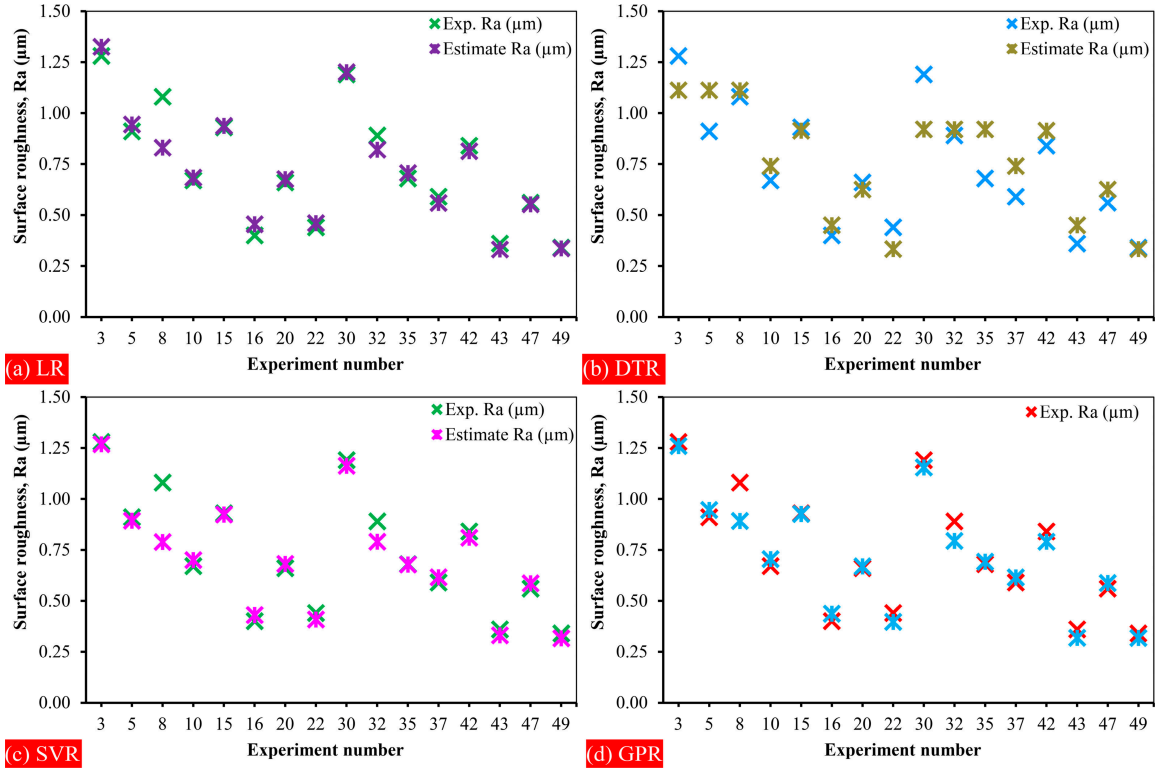

Figure 19. Comparison of experimental and predicted results for surface roughness.

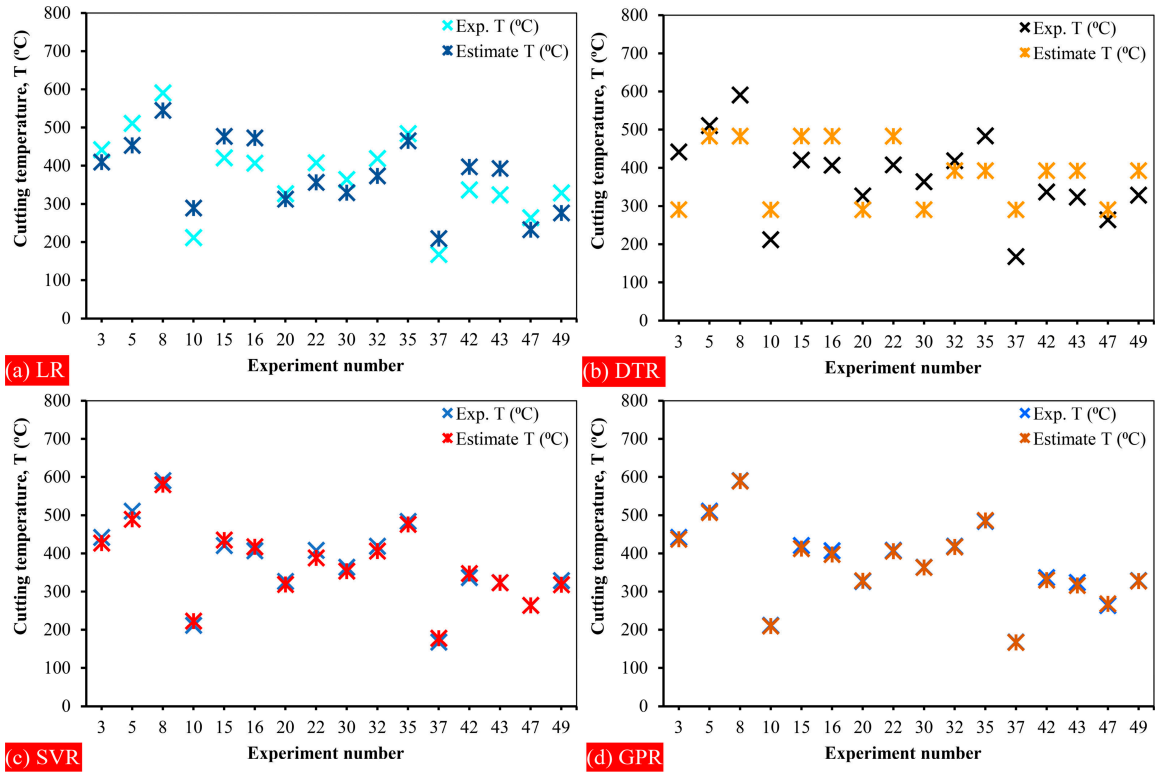

Figure 20. Comparison of experimental and predicted results for cutting temperature.

Table 4. Accuracy rates of the model prediction results.

Models	Fc	Ra	T
Linear regression	83.1107	94.6299	85.9538
Decision tree regression	88.6217	85.8098	78.5059
Support vector regression	93.6496	94.0772	96.9987
Gaussian Process Regression	98.7257	93.9117	98.9967

The performance of machine learning models was compared using four different evaluation metrics (MAE, MSE, RMSE, and R^2), and the results are presented in Table 5. Examination of Table 5 shows that the LR, DTR, SVR, and GPR methods generally achieved high model accuracy in predicting cutting force, surface roughness, and cutting temperature parameters. The high R^2 values and low MAE, MSE, and RMSE values indicate that the prediction performance of these models is reliable and acceptable.

Table 5. Percentage error results of the predicted output parameters using four regression-based machine learning models.

	LR	DTC	SVR	GPR	LR	DTC	SVR	GPR
	Fc Performances				**Ra Performances**			
MAE	6.1335	4.1592	2.5773	0.5313	0.0025	0.0063	0.0028	0.0027
MSE	813.6914	385.3602	220.5018	9.2690	0.000304	0.01024	0.000403	0.00227
RMSE	24.5338	16.6370	10.3091	2.1251	0.0106	0.0251	0.0110	0.0101
R^2	0.6362	0.8277	0.9014	0.9959	0.9394	0.7963	0.9198	0.9548
	T performances							
MAE	2.9385	4.4696	0.6795	0.2289				
MSE	156.5673	391.4249	9.1655	1.3269				
RMSE	11.7540	17.8785	2.7181	0.9155				
R^2	0.7748	0.4371	0.9868	0.9981				

5. Conclusions

In this study, the microstructural properties, mechanical properties, and machinability performance of Inconel 718 alloys produced by forging and Selective Laser Melting (SLM) methods, as well as samples subjected to heat treatment after SLM, were comprehensively evaluated. The effects of microstructure, mechanical properties, cutting parameters, and machining conditions on cutting force, surface roughness, cutting temperature, and tool wear were experimentally investigated. The performance of machine learning models developed using the obtained data in predicting process outputs was examined in detail. The main results obtained within the scope of the study are summarized below.

- The WP1 sample, produced by the forging method, showed the highest hardness (457 Hv) and relative density (99.886%) values thanks to its fine-grained and homogeneous microstructure. In contrast, the WP2 sample, produced by SLM, showed a decrease in hardness to 303.33 Hv and a decrease in relative density of approximately 1.98% due to the formation of dendritic structure and porosity. In the heat-treated WP3 sample, the hardness increased to 391 Hv and an improvement in density of approximately 0.40% was achieved due to the effect of γ' and γ'' precipitates.
- The lowest cutting force value was obtained in the WP2 specimen under MQL conditions, while the highest cutting force value was obtained in the WP1 specimen under dry machining. In general, increasing the cutting speed reduced the cutting forces, while increasing the feed rate significantly increased the cutting forces.

- MQL application reduced the average cutting force by approximately 15.5% compared to dry machining. This was attributed to reduced friction and temperature.
- The lowest Ra value was obtained in the WP3 sample, and the highest value in the WP1 sample. MQL application improved surface quality. The lubricant film layer reduced friction and adhesion.
- The lowest cutting temperature was observed in the WP2 sample, and the highest in the WP1 sample under dry machining conditions. The MQL application reduced the cutting temperature by an average of 18.65% compared to dry machining. This is explained by better lubrication and heat transfer.
- The highest tool wear was observed in the WP1 specimen. Under dry machining conditions, adhesion, abrasive wear, and coating peeling were the dominant wear mechanisms.
- The highest success rate among machine learning models was achieved with the GPR model. The GPR model provided 98.72% accuracy for cutting force and 98.99% accuracy for cutting temperature. In surface roughness prediction, the most successful model was LR.

Author Contributions: Conceptualization, F.C. and B.Ö.; methodology, F.C., B.Ö. and H.D.; software, B.Ö. and F.K.; validation, B.Ö., H.D. and F.K.; investigation, F.C., B.Ö., H.D. and F.K.; resources, F.C. and B.Ö.; data curation, F.C. and B.Ö.; writing—original draft preparation, F.C., B.Ö. and F.K.; writing—review and editing, F.C., B.Ö. and F.K.; visualization, F.C., B.Ö. and F.K.; supervision, B.Ö., H.D. and F.K. All authors have read and agreed to the published version of the manuscript.

Funding: This research received no external funding.

Data Availability Statement: The original contributions presented in this study are included in the article; further inquiries can be directed to the corresponding authors.

Acknowledgments: This study was supported by the Scientific Research Projects Coordination Unit of Karabük University (Project No: KBÜBAP-25-KP-044). The authors would like to thank the Scientific Research Projects Coordination Unit of Karabük University for their support.

Conflicts of Interest: The authors declare no conflicts of interest.

Abbreviations

The following abbreviations are used in this manuscript:

Vc	Cutting Speed
f	Feed Rate
ap	Depth of Cut
MQL	Minimum Quantity Lubrication
BUE	Built-Up Edge
Vb	Flank Wear
SEM	Scanning Electron Microscope
SLM	Selective Laser Melting
LR	Linear Regression
DTR	Decision Tree Regression
SVR	Support Vector Regression
GPR	Gaussian Process Regression
MAPE	Mean Absolute Percentage Error
MAE	Mean Absolute Error
RMSE	Root Mean Square Error
R^2	Coefficient of Determination

References

1. Şahin, A.; Özlü, B.; Demir, H.; Gündüz, S. Experimental investigation and optimization of the effects of SLM parameters on surface quality, geometric tolerances, microstructure and mechanical properties of CoCrMo dental alloys. *Proc. Inst. Mech. Eng. Part C J. Mech. Eng. Sci.* **2026**, *240*, 413454.
2. Zhang, J.; Meng, G.; Zhu, L.; Xu, P.; Wang, S.; Xue, P.; Yang, Z. Research on the evolution mechanism of solidified structure during laser cladding IN718 alloy. *Appl. Therm. Eng.* **2022**, *215*, 118925. [CrossRef]
3. Günay, M.; Gündüz, S.; Yılmaz, H.; Yaşar, N.; Kaçar, R. Optimization of 3D printing operation parameters for tensile strength in PLA based sample. *J. Polytech.* **2020**, *23*, 73–79.
4. Sheng, L.; Jiao, J.; Zhao, H. Materials, processing, and post-treatment for metal-based additive manufacturing. *Materials* **2025**, *18*, 4311. [PubMed]
5. Işik, U.; Demir, H.; Özlü, B. Multi-objective optimization of process parameters for surface quality and geometric tolerances of AlSi10Mg samples produced by additive manufacturing method using Taguchi-based gray relational analysis. *Arab. J. Sci. Eng.* **2025**, *50*, 9211–9229.
6. Yap, C.Y.; Chua, C.K.; Dong, Z.L.; Liu, Z.H.; Zhang, D.Q.; Loh, L.E.; Sing, S.L. Review of selective laser melting: Materials and applications. *Appl. Phys. Rev.* **2015**, *2*, 041101. [CrossRef]
7. Jia, Q.; Gu, D. Selective laser melting additive manufacturing of Inconel 718 superalloy parts: Densification, microstructure and properties. *J. Alloys Compd.* **2014**, *585*, 713–721. [CrossRef]
8. Moussaoui, K.; Rubio, W.; Mousseigne, M.; Sultan, T.; Rezai, F. Effects of Selective Laser Melting additive manufacturing parameters of Inconel 718 on porosity, microstructure and mechanical properties. *Mater. Sci. Eng. A* **2018**, *735*, 182–190. [CrossRef]
9. Nnaji, R.N.; Bodude, M.A.; Osoba, L.O.; Fayomi, O.S.I.; Ochulor, F.E. Study on high-temperature oxidation kinetics of Haynes 282 and Inconel 718 nickel-based superalloys. *Int. J. Adv. Manuf. Technol.* **2020**, *106*, 1149–1160.
10. Tucho, W.M.; Cuvillier, P.; Sjolyst-Kverneland, A.; Hansen, V. Microstructure and hardness studies of Inconel 718 manufactured by selective laser melting before and after solution heat treatment. *Mater. Sci. Eng. A* **2017**, *689*, 220–232. [CrossRef]
11. Turan, İ.; Özlü, B.; Ulaş, H.B.; Demir, H. Prediction and modelling with Taguchi, ANN and ANFIS of optimum machining parameters in drilling of Al 6082–T6 alloy. *J. Manuf. Mater. Process.* **2025**, *9*, 92.
12. Hamıd, M.W.H.; Özlü, B.; Ulaş, H.B.; Demir, H. Prediction of cutting parameters and reduction of output parameters using machine learning in milling of Inconel 718 alloy. *Sci. Rep.* **2025**, *15*, 33309. [CrossRef] [PubMed]
13. Şap, S.; Acar, E.; Değirmenci, Ü.; Usca, Ü.A.; Memiş, S.; Şener, R. Machinability of different Cu-Gr composites in milling: Performance parameters prediction via machine learning models. *Expert Syst. Appl.* **2025**, *272*, 126770. [CrossRef]
14. Özkan, E.K.; Ulaş, H.B. Comparison of four machine learning methods for occupational accidents based on national data on metal sector in Turkey. *Saf. Sci.* **2024**, *174*, 106468. [CrossRef]
15. Li, C.; Wang, K.; Piao, Y.; Cui, H.; Zakharov, O.; Duan, Z.; Zhang, F.; Yan, Y.; Geng, Y. Surface micro-morphology model involved in grinding of GaN crystals driven by strain-rate and abrasive coupling effects. *Int. J. Mach. Tools Manuf.* **2024**, *201*, 104197.
16. Pérez-Ruiz, J.D.; de Lacalle, L.N.L.; Urbikain, G.; Pereira, O.; Martínez, S.; Bris, J. On the relationship between cutting forces and anisotropy features in the milling of LPBF Inconel 718 for near net shape parts. *Int. J. Mach. Tools Manuf.* **2021**, *170*, 103801. [CrossRef]
17. Ji, H.; Gupta, M.K.; Song, Q.; Cai, W.; Zheng, T.; Zhao, Y.; Pimenov, D.Y. Microstructure and machinability evaluation in micro milling of selective laser melted Inconel 718 alloy. *J. Mater. Res. Technol.* **2021**, *14*, 348–362. [CrossRef]
18. Natarajan, S.P.; Vaudreuil, S.; Chibane, H.; Morandeau, A.; Xavior, M.A.; Cormier, J.; Duchosal, A. Influence of heat treatment on the tool life while machining SLM Inconel 718 with reference to C&W Inconel 718. *J. Manuf. Process.* **2022**, *83*, 192–202. [CrossRef]
19. Schulze, P.; Sammler, F.; Pfennig, A.; Heiler, R. Investigation of milling tools for machining Inconel 718 parts produced by selective laser melting. *Procedia CIRP* **2023**, *118*, 555–559. [CrossRef]
20. Bagherzadeh, A.; Budak, E.; Ozlu, E.; Koc, B. Machining behavior of Inconel 718 in hybrid additive and subtractive manufacturing. *CIRP J. Manuf. Sci. Technol.* **2023**, *46*, 178–190. [CrossRef]
21. Periane Natarajan, S.; Vaudreuil, S.; Chibane, H.; Morandeau, A.; Xavior, M.A.; Cormier, J.; Duchosal, A. Tool life and surface integrity characteristics in milling of SLM and C&W inconel 718 in dry and MQL condition. *Int. J. Adv. Manuf. Technol.* **2022**, *121*, 647–659. [CrossRef]
22. Khanna, N.; Prajapati, R.; Badheka, V.; Fuse, K.A.; Singh, M.; Palanisamy, S. Influence of tool geometry and coatings on high-speed drilling performance of additively manufactured Inconel 718. *J. Tribol.* **2026**, *148*, 072504. [CrossRef]
23. Careri, F.; Umbrello, D.; Essa, K.; Attallah, M.M.; Imbrogno, S. The effect of the heat treatments on the tool wear of hybrid additive manufacturing of IN718. *Wear* **2021**, *470*, 203617.
24. Chen, L.; Xu, Q.; Liu, Y.; Cai, G.; Liu, J. Machinability of the laser additively manufactured Inconel 718 superalloy in turning. *Int. J. Adv. Manuf. Technol.* **2021**, *114*, 871–882. [CrossRef]
25. Tian, C.; Li, X.; Liu, Z.; Zhi, G.; Guo, G.; Wang, L.; Rong, Y. Study on grindability of Inconel 718 superalloy fabricated by selective laser melting (SLM). *Stroj. Vestn. J. Mech. Eng.* **2018**, *64*, 319–328. [CrossRef]

26. Calleja, A.; Urbikain, G.; González, H.; Cerrillo, I.; Polvorosa, R.; Lamikiz, A. Inconel® 718 superalloy machinability evaluation after laser cladding additive manufacturing process. *Int. J. Adv. Manuf. Technol.* **2018**, *97*, 2873–2885.
27. Kaynak, Y.; Tascioglu, E. Finish machining-induced surface roughness, microhardness and XRD analysis of selective laser melted Inconel 718 alloy. *Procedia CIRP* **2018**, *71*, 500–504. [CrossRef]
28. Kappes, B.; Moorthy, S.; Drake, D.; Geerlings, H.; Stebner, A. Machine learning to optimize additive manufacturing parameters for laser powder bed fusion of Inconel 718. In *Proceedings of the 9th International Symposium on Superalloy 718 & Derivatives: Energy, Aerospace, and Industrial Applications*; Springer International Publishing: Cham, Switzerland, 2018; pp. 595–610.
29. Sah, A.K.; Agilan, M.; Dineshraj, S.; Rahul, M.R.; Govind, B. Machine learning-enabled prediction of density and defects in additively manufactured Inconel 718 alloy. *Mater. Today Commun.* **2022**, *30*, 103193. [CrossRef]
30. Yu, Z.; Lu, C.; Maitra, V.; Shi, J. Machine learning-enabled predictions for tensile strength of laser additively manufactured Inconel 718 alloy. *Int. J. Adv. Manuf. Technol.* **2026**, *142*, 1695–1716.
31. Ravichander, B.B.; Rahimzadeh, A.; Farhang, B.; Shayesteh Moghaddam, N.; Amerinatanzi, A.; Mehrpouya, M. A prediction model for additive manufacturing of inconel 718 superalloy. *Appl. Sci.* **2021**, *11*, 8010. [CrossRef]
32. Frank, L.E.; Friedman, J.H. A statistical view of some chemometrics regression tools. *Technometrics* **1993**, *35*, 109–135. [CrossRef]
33. Dubey, V.; Sharma, A.K.; Kumar, H.; Arora, P.K. Prediction of cutting forces in MQL turning of AISI 304 Steel using machine learning algorithm. *J. Eng. Res.* **2022**, 1–13. [CrossRef]
34. Flores, V.; Keith, B. Gradient Boosted Trees Predictive Models for Surface Roughness in High-Speed Milling in the Steel and Aluminum Metalworking Industry. *Complexity* **2019**, *2019*, 1536716.
35. Kuntoğlu, M.; Demirpolat, H.; Binali, R.; Korkmaz, M.E.; Makhesana, M.; Kaya, K. Sustainable lubrication strategies in eco-friendly machining of AISI 4140 steel: Performance and environmental impact analysis using machine learning. *J. Mater. Eng. Perform.* **2022**, *35*, 4962–4978.
36. Jurkovic, Z.; Cukor, G.; Brezocnik, M.; Brajkovic, T. A comparison of machine learning methods for cutting parameters prediction in high-speed turning process. *J. Intell. Manuf.* **2018**, *29*, 1683–1693.
37. Hashemitaheri, M.; Mekarthy, S.M.R.; Cherukuri, H. Prediction of specific cutting forces and maximum tool temperatures in orthogonal machining by support vector and Gaussian process regression methods. *Procedia Manuf.* **2020**, *48*, 1000–1008. [CrossRef]
38. Chen, J.; Lin, J.; Zhang, M.; Lin, Q. Predicting surface roughness in turning complex-structured workpieces using vibration-signal-based gaussian process regression. *Sensors* **2024**, *24*, 2117. [PubMed]
39. Makhfi, S.; Dorbane, A.; Harrou, F.; Sun, Y. Prediction of cutting forces in hard turning process using machine learning methods: A case study. *J. Mater. Eng. Perform.* **2024**, *33*, 9095–9111.
40. Alajmi, M.S.; Almeshal, A.M. Modeling of cutting force in the turning of aisi 4340 using gaussian process regression algorithm. *Appl. Sci.* **2021**, *11*, 4055. [CrossRef]
41. Zhang, R.Y.; Qin, H.L.; Bi, Z.N.; Li, J.; Paul, S.; Lee, T.L.; Zhang, S.Y.; Zhang, J.; Dong, H.B. Evolution of lattice spacing of gamma double prime precipitates during aging of polycrystalline Ni-base superalloys: An in situ investigation. *Metall. Mater. Trans. A* **2020**, *51*, 574–585.
42. Ahmadi, M.R.; Rath, M.; Povoden-Karadeniz, E.; Primig, S.; Wojcik, T.; Danninger, A.; Stockinger, M.; Kozeschnik, E. Modeling of precipitation strengthening in Inconel 718 including non-spherical γ'' precipitates. *Modell. Simul. Mater. Sci. Eng.* **2017**, *25*, 055005.
43. Wu, J.; Cheng, Y.; Su, J.; Ke, Y.; Teng, J.; Jiang, F. Comparative Study on ıntermediate-temperature deformation mechanisms of Inconel 718 alloys fabricated by additive manufacturing and conventional forging. *Materials* **2025**, *18*, 5354. [PubMed]
44. Balan, A.; Perez, M.; Chaise, T.; Cazottes, S.; Bardel, D.; Corpace, F.; Nelias, D. Precipitation of γ''in Inconel 718 alloy from microstructure to mechanical properties. *Materialia* **2021**, *20*, 101187.
45. Wang, X.; Gong, X.; Chou, K. Review on powder-bed laser additive manufacturing of Inconel 718 parts. *Proc. Inst. Mech. Eng. Part B J. Eng. Manuf.* **2017**, *231*, 1890–1903.
46. Yu, X.; Lin, X.; Liu, F.; Wang, L.; Tang, Y.; Li, J.; Zhang, S.; Huang, W. Influence of post-heat-treatment on the microstructure and fracture toughness properties of Inconel 718 fabricated with laser directed energy deposition additive manufacturing. *Mater. Sci. Eng. A* **2020**, *798*, 140092.
47. Amato, K.N.; Gaytan, S.M.; Murr, L.E.; Martinez, E.; Shindo, P.W.; Hernandez, J.; Collins, C.; Medina, F. Microstructures and mechanical behavior of Inconel 718 fabricated by selective laser melting. *Acta Mater.* **2012**, *60*, 2229–2239. [CrossRef]
48. Chlebus, E.; Gruber, K.; Kuźnicka, B.; Kurzac, J.; Kurzynowski, T. Effect of heat treatment on the microstructure and mechanical properties of Inconel 718 processed by selective laser melting. *Mater. Sci. Eng. A* **2015**, *639*, 647–655. [CrossRef]
49. Parida, A.K. Analysis of chip geometry in hot machining of Inconel 718 alloy. *Iran. J. Sci. Technol. Trans. Mech. Eng.* **2019**, *43*, 155–164.
50. Parida, A.K.; Maity, K. Effect of nose radius on forces, and process parameters in hot machining of Inconel 718 using finite element analysis. *Eng. Sci. Technol. Int. J.* **2017**, *20*, 687–693. [CrossRef]

51. Thakur, D.G.; Ramamoorthy, B.; Vijayaraghavan, L. Study on the machinability characteristics of superalloy Inconel 718 during high speed turning. *Mater. Des.* **2009**, *30*, 1718–1725. [CrossRef]
52. Hao, Z.; Fan, Y.; Lin, J.; Ji, F.; Liu, X. New observations on wear mechanism of self-reinforced SiAlON ceramic tool in milling of Inconel 718. *Arch. Civ. Mech. Eng.* **2017**, *17*, 467–474.
53. Gupta, M.K.; Mia, M.; Pruncu, C.I.; Kapłonek, W.; Nadolny, K.; Patra, K.; Sharma, V.S. Parametric optimization and process capability analysis for machining of nickel-based superalloy. *Int. J. Adv. Manuf. Technol.* **2019**, *102*, 3995–4009. [CrossRef]
54. Bai, W.; Bisht, A.; Roy, A.; Suwas, S.; Sun, R.; Silberschmidt, V.V. Improvements of machinability of aerospace-grade Inconel alloys with ultrasonically assisted hybrid machining. *Int. J. Adv. Manuf. Technol.* **2019**, *101*, 1143–1156.
55. Çakıroğlu, R. Machinability analysis of Inconel 718 superalloy with AlTiN-coated carbide tool under different cutting environments. *Arab. J. Sci. Eng.* **2021**, *46*, 8055–8073.
56. Özlü, B.; Ulaş, H.B.; Kara, F. Investigation of the effects of cutting tool coatings and machining conditions on cutting force, specific energy consumption, surface roughness, cutting temperature, and tool wear in the milling of Ti6Al4V alloy. *Lubricants* **2025**, *13*, 363.
57. Talib, N.; Rahim, E.A. Performance of modified jatropha oil in combination with hexagonal boron nitride particles as a bio-based lubricant for green machining. *Tribol. Int.* **2018**, *118*, 89–104. [CrossRef]
58. Attanasio, A.; Gelfi, M.; Giardini, C.; Remino, C. Minimal quantity lubrication in turning: Effect on tool wear. *Wear* **2006**, *260*, 333–338. [CrossRef]
59. Dhar, N.R.; Kamruzzaman, M.; Ahmed, M. Effect of minimum quantity lubrication (MQL) on tool wear and surface roughness in turning AISI-4340 steel. *J. Mater. Process. Technol.* **2006**, *172*, 299–304. [CrossRef]
60. Akkuş, H.; Yaka, H. Experimental and statistical investigation of the effect of cutting parameters on surface roughness, vibration and energy consumption in machining of titanium 6Al-4V ELI (grade 5) alloy. *Measurement* **2021**, *167*, 108465. [CrossRef]
61. Kara, F. Investigation of the effect of Al2O3 nanoparticle-added MQL lubricant on sustainable and clean manufacturing. *Lubricants* **2024**, *12*, 393.
62. Kara, F.; Karabatak, M.; Ayyıldız, M.; Nas, E. Effect of machinability, microstructure and hardness of deep cryogenic treatment in hard turning of AISI D2 steel with ceramic cutting. *J. Mater. Res. Technol.* **2020**, *9*, 969–983. [CrossRef]
63. Kawasaki, K. High-Efficiency Milling of Inconel 718 Superalloy: Effects of Cutting Conditions on Tool Life and Surface Roughness. *Machines* **2025**, *13*, 974. [CrossRef]
64. Wu, T.Y.; Lin, C.C. Optimization of machining parameters in milling process of Inconel 718 under surface roughness constraints. *Appl. Sci.* **2021**, *11*, 2137. [CrossRef]
65. Ahmaida, Y.A.A.; Akgün, M.; Erden, M.A. Fabrication, characterization, and MQL assisted machining of layered functionally graded 316L/Distaloy AB composites by powder metallurgy method. *Eng. Sci. Technol. Int. J.* **2026**, *78*, 102352. [CrossRef]
66. Ünlü, E.; Akgün, M.; Demir, H. Multi-objective optimization of process parameters in electro discharge machining of Inconel 625 superalloy with different electrode materials. *Mater. Test.* **2026**, *68*, 306–322. [CrossRef]
67. Binali, R. Experimental and machine learning comparison for measurement the machinability of nickel based alloy in pursuit of sustainability. *Measurement* **2024**, *236*, 115142. [CrossRef]
68. Khan, M.M.A.; Mithu, M.A.H.; Dhar, N.R. Effects of minimum quantity lubrication on turning AISI 9310 alloy steel using vegetable oil-based cutting fluid. *J. Mater. Process. Technol.* **2009**, *209*, 5573–5583. [CrossRef]
69. De Bartolomeis, A.; Newman, S.T.; Shokrani, A. High-speed milling Inconel 718 using electrostatic minimum quantity lubrication (EMQL). *Procedia CIRP* **2021**, *101*, 354–357. [CrossRef]
70. Makhesana, M.A.; Patel, K.M.; Bagga, P.J. Evaluation of surface roughness, tool wear and chip morphology during machining of nickel-based alloy under sustainable hybrid nanofluid-MQL strategy. *Lubricants* **2022**, *10*, 315.
71. Zheng, J.; Zhang, Y.; Qiao, H. Milling Mechanism and Chattering Stability of Nickel-Based Superalloy Inconel 718. *Materials* **2023**, *16*, 5748. [CrossRef] [PubMed]
72. Fernandes, G.H.N.; Barbosa, L.M.Q.; França, P.H.P.; Ferreira, E.R.; Martins, P.S.; Machado, Á.R. Enhancing sustainability in Inconel 718 machining: Temperature control with internally cooled tools. *Int. J. Adv. Manuf. Technol.* **2024**, *131*, 2771–2789.
73. Karagöz, C.; Özlü, B.; Ulaş, H.B.; Demir, H. RSM ANN and ANFIS based analysis of machining conditions and cutting parameters in sustainable milling of AISI 316 Ti alloy. *Multidiscip. Model. Mater. Struct.* **2026**, *22*, 132–159.
74. Groover, M.P. *Fundamentals of Modern Manufacturing: Materials, Processes, and Systems*; John Wiley & Sons: Hoboken, NJ, USA, 2010.
75. Shokrani, A.; Dhokia, V.; Newman, S.T. Environmentally conscious machining of difficult-to-machine materials with regard to cutting fluids. *Int. J. Mach. Tools Manuf.* **2012**, *57*, 83–101.

Disclaimer/Publisher's Note: The statements, opinions and data contained in all publications are solely those of the individual author(s) and contributor(s) and not of MDPI and/or the editor(s). MDPI and/or the editor(s) disclaim responsibility for any injury to people or property resulting from any ideas, methods, instructions or products referred to in the content.